NASA TM X-106

ification changed to declassifie
ective 1 April 1963
ority of NASA CCN 2 by
Carroll

N63-13892

TECHNICAL MEMORANDUM
X-106

Code-1

TRANSONIC STATIC AERODYNAMIC CHARACTERISTICS OF A BLUNT

CONE-CYLINDER BODY WITH FLARED AFTERBODIES

OF VARIOUS ANGLES AND BASE AREAS

By Roy M. Wakefield, Earl D. Knechtel,
and Stuart L. Treon

Ames Research Center
Moffett Field, Calif.

553982

NATIONAL AERONAUTICS AND SPACE ADMINISTRATION

WASHINGTON December 1959

CONFIDENTIAL

NATIONAL AERONAUTICS AND SPACE ADMINISTRATION

TECHNICAL MEMORANDUM X-106

TRANSONIC STATIC AERODYNAMIC CHARACTERISTICS OF A BLUNT

CONE-CYLINDER BODY WITH FLARED AFTERBODIES

OF VARIOUS ANGLES AND BASE AREAS*

By Roy M. Wakefield, Earl D. Knechtel,
and Stuart L. Treon

SUMMARY

A transonic wind-tunnel investigation has been conducted to determine the static aerodynamic characteristics of a low-fineness-ratio blunt cone-cylinder stabilized by various flared afterbodies. The effects of variation of the ratio of flare base area to body cross-sectional area are shown for three flare angles. Test Mach numbers ranged from 0.60 to 1.40 and angles of attack from -2° to $+14^{\circ}$, for a constant Reynolds number of 0.375 million based upon the cylindrical body diameter.

INTRODUCTION

Recent increased demand for aerodynamic data on low-fineness-ratio bodies of revolution at transonic speeds stems not only from the growing interest in atmosphere entry vehicles and aircraft escape capsules, but also from an increasing awareness that stability of such bodies is often critical in the transonic speed range. Experimental studies of low-fineness-ratio blunt bodies at transonic speeds, such as that of reference 1, are not sufficiently numerous to provide data over the ranges of design parameters of interest.

As part of a continuing study at the Ames Research Center of the transonic aerodynamic characteristics of low-fineness-ratio bodies (the first results of which are reported in ref. 2), results are presented for a blunt cone-cylinder with various flared afterbodies. The present report shows the effects of varying the ratio of flare base area to body cross-sectional area from 2 to 6 for flare angles of 10°, 20°, and 30°. The results are presented without detailed discussion.

---

*Title, Unclassified

NOTATION

B   base area of flared afterbody

C_{A_b} base axial-force coefficient, $\dfrac{\text{base axial force}}{qS}$

C_{A_f} forebody axial-force coefficient, $\dfrac{\text{forebody axial force}}{qS}$

C_m pitching-moment coefficient about nose-cylinder juncture, $\dfrac{\text{pitching moment}}{qSd}$

C_N normal-force coefficient, $\dfrac{\text{normal force}}{qS}$.

$\dfrac{C_N}{\alpha}$ normal-force parameter, that is, the slope of the straight line drawn from C_N at $\alpha = 0^\circ$ to any point on the C_N vs. α curve

c.p.   center of pressure

d   cylindrical body diameter

L   model length

L_f flare length

M   Mach number

q   dynamic pressure

S   cross-sectional area of cylindrical body

α angle of attack, deg

θ flare semivertex angle, deg

Model Component Designations

N_2 blunt conical nose

B_2 cylindrical body, subscript indicating length in diameters

F_{xx-x} flared afterbody, subscript **xx** indicating flare semivertex angle in degrees, and subscript **x** indicating ratio of flare base area to cylindrical body cross-sectional area

3

APPARATUS AND MODELS

The investigation was conducted in the Ames 2- by 2-foot transonic wind tunnel which is equipped with a perforated test section affording continuous choke-free operation at Mach numbers up to 1.4. Additional information regarding this test facility is provided in reference 3.

Dimensioned sketches of the 13 models employed in this investigation are shown in figure 1. Common to all of the models were a blunt conical nose and cylindrical center body 2 diameters in length. This basic shape was tested alone and with various flared afterbodies. Flare angles were 10°, 20°, and 30°; flare lengths were as required to provide ratios of flare base area to body cross-sectional area of 2, 3, 4, and 6. A boundary-layer trip wire 0.008 inch in diameter was cemented around the conical surface 1/2 inch behind the tip of the nose (fig. 1).

The models were mounted in the wind-tunnel test section on a sting-supported, internal, strain-gage balance. Photographs of two of the models installed in the test section are shown in figure 2.

TESTS, DATA REDUCTION, AND PRECISION

The investigation was conducted at ten Mach numbers from 0.6 to 1.4, eleven angles of attack from -2^O to $+14^O$, and a constant Reynolds number of 0.375 million based on the cylindrical body diameter. Normal force, axial force, and pitching moment were determined for all models.

Preliminary studies employing the boundary-layer visualization technique of reference 4 indicated that the boundary-layer flow over the blunt conical nose naturally became turbulent on the fore part of the conical surface; hence the boundary layer would also be expected to be turbulent at the higher Reynolds numbers of full-scale flight conditions. To ensure uniformly turbulent boundary-layer conditions, an 0.008-inch-diameter trip wire was employed on the conical nose surface (fig. 1) and was observed to be effective by the previously mentioned boundary-layer visualization technique.

The axial forces were resolved to forebody and base axial-force coefficients. For the forebody axial-force coefficients, the measured axial forces were adjusted to account for the difference between the measured base pressure and an assumed condition of free-stream static pressure acting at the base of the model.

The results of references 5 and 6 for models having cylindrical and flared afterbodies indicate significant effects of the presence of a sting on base axial force, whereas there is evidence that the forebody

axial force is not affected. The magnitudes of such effects on base
axial force are not known for the present models; therefore, the base
axial-force coefficients do not necessarily represent the actual forces
that would be encountered in free flight.

The angles of attack have been corrected for elastic deflection of
the balance and sting under aerodynamic loads. Stream-angularity cor-
rections in this wind tunnel are known to be negligible and therefore
were not applied.

No corrections have been made for possible interference effects of
the perforated test-section walls inasmuch as transonic tests of various
sizes of sharp- and blunt-nosed bodies reported in the appendix to refer-
ence 7 indicated no significant systematic effects of wall interference.
However, there was an indication at a Mach number of 1.2 of reflected
wave interference on the base axial-force coefficients for two models
with large flares.

In addition to the possible systematic errors resulting from
neglecting some of the above effects, certain random errors exist which
influence the precision, or repeatability, of the results. An analysis
using the methods of reference 8 indicated that the precisions of Mach
number, angle of attack, and aerodynamic coefficients were as follows:

$$M \quad 0.003 \qquad C_m \quad 0.03$$

$$\alpha \quad 0.05^{\circ} \qquad C_{A_f} \quad 0.02$$

$$C_N \quad 0.02 \qquad C_{A_b} \quad 0.01$$

RESULTS

The variations with angle of attack of coefficients of normal force,
pitching moment, forebody axial force, and base axial force for a blunt
cone-cylinder with various flared afterbodies are presented in figures 3
to 14. The variations with Mach number of normal-force parameter C_N/α
and center of pressure at selected angles of attack, and of forebody and
base axial-force coefficients at 0° angle of attack are summarized in
figures 15 to 21. Shadowgraph views of two flared models are presented
in figure 22 to show the difference in shock patterns and flow separation
ahead of the flares for two sizes of flares at two Mach numbers. The
separation was observed to have a significant effect on the longitudinal
characteristics of the larger models, particularly on the normal-force
parameter (fig. 19) and center of pressure (fig. 20).

The decrease in the level of the base axial-force coefficients at
a Mach number of 1.2 for the models with the largest 20° and 30° flares

5

(figs. 10 and 18(b) and figs. 14 and 18(c), respectively) are presumed to result from wall-reflected disturbances. The estimated level of C_{A_b} in the region of the presumed interference is shown by a broken line (figs. 18(b),(c)). No effects of the disturbances were evident on the corresponding normal-force, pitching-moment, and forebody axial-force coefficients.

Ames Research Center
    National Aeronautics and Space Administration
        Moffett Field, Calif., July 9, 1959

REFERENCES

1. Fisher, Lewis R., Keith, Arvid R., Jr., and DiCamillo, Joseph R.: Aerodynamic Characteristics of Some Families of Blunt Bodies at Transonic Speeds. NASA MEMO 10-28-58L, 1958.

2. Knechtel, Earl D., Treon, Stuart L., and Wakefield, Roy M.: Transonic Static Aerodynamic Characteristics of a Blunt Cone-Cylinder Body With Flared Afterbody or Blunt Cruciform Fins. NASA TM X-40, 1959.

3. Spiegel, Joseph M., and Lawrence, Leslie F.: A Description of the Ames 2- by 2-Foot Transonic Wind Tunnel and Preliminary Evaluation of Wall Interference. NACA RM A55I21, 1956.

4. Main-Smith, J. D.: Chemical Solids as Diffusible Coating Films for Visual Indications of Boundary-Layer Transition in Air and Water. R. & M. No. 2755, British A.R.C., 1954.

5. Lee, George, and Summers, James L.: Effects of Sting-Support Interference on the Drag of an Ogive-Cylinder Body With and Without a Boattail at 0.6 to 1.4 Mach Number. NACA RM A57I09, 1957.

6. Reese, David E., Jr., and Wehrend, William R., Jr.: Effects of Sting-Support Interference on the Base Pressures of a Model Having a Blunt-Nosed Cylinder Body and a Conical Flare at Mach Numbers of 0.65 to 2.20. NASA TM X-161, 1959.

7. Treon, Stuart L.: The Effect of Nose Shape on the Static Aerodynamic Characteristics of Ballistic-Type Missile Models at Mach Numbers From 0.6 to 1.4. NASA MEMO 5-17-59A, 1959.

8. Beers, Yardley: Introduction to the Theory of Error. Addison-Wesley Pub. Co., Cambridge, Mass., 1953.

MODEL	θ, Deg.	L/d	B/S	L_f/d
N_2B_2	——	3.22	1	0.00
$N_2B_2F_{10-2}$	10	4.39	2	1.17
$N_2B_2F_{10-3}$	10	5.29	3	2.07
$N_2B_2F_{10-4}$	10	6.06	4	2.84
$N_2B_2F_{10-6}$	10	7.33	6	4.11
$N_2B_2F_{20-2}$	20	3.78	2	0.56
$N_2B_2F_{20-3}$	20	4.22	3	1.00
$N_2B_2F_{20-4}$	20	4.59	4	1.37
$N_2B_2F_{20-6}$	20	5.21	6	1.99
$N_2B_2F_{30-2}$	30	3.60	2	0.38
$N_2B_2F_{30-3}$	30	3.84	3	0.62
$N_2B_2F_{30-4}$	30	4.08	4	0.86
$N_2B_2F_{30-6}$	30	4.46	6	1.24

All dimensions in inches unless otherwise noted.
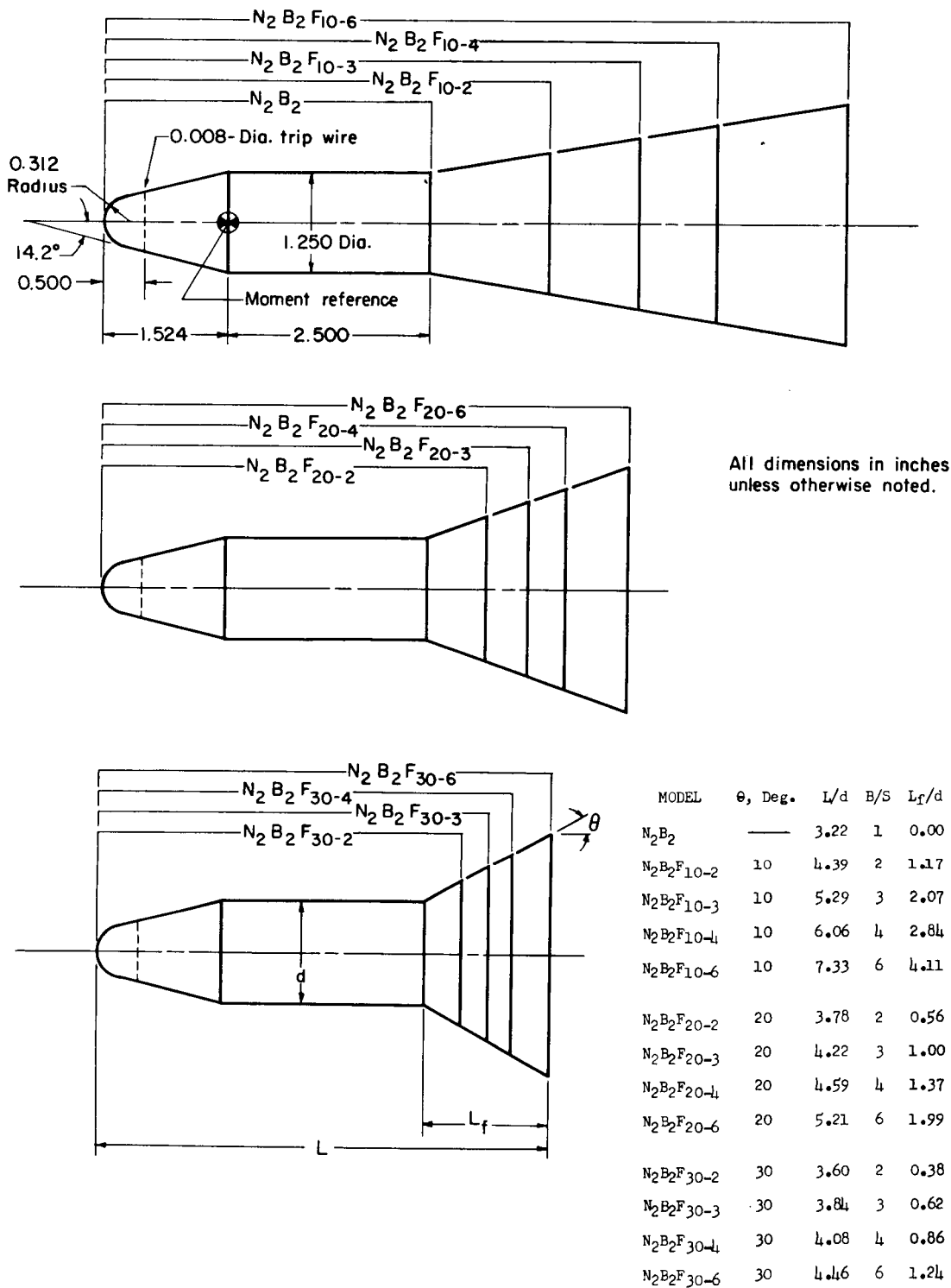
Figure 1.- Geometric details of models.
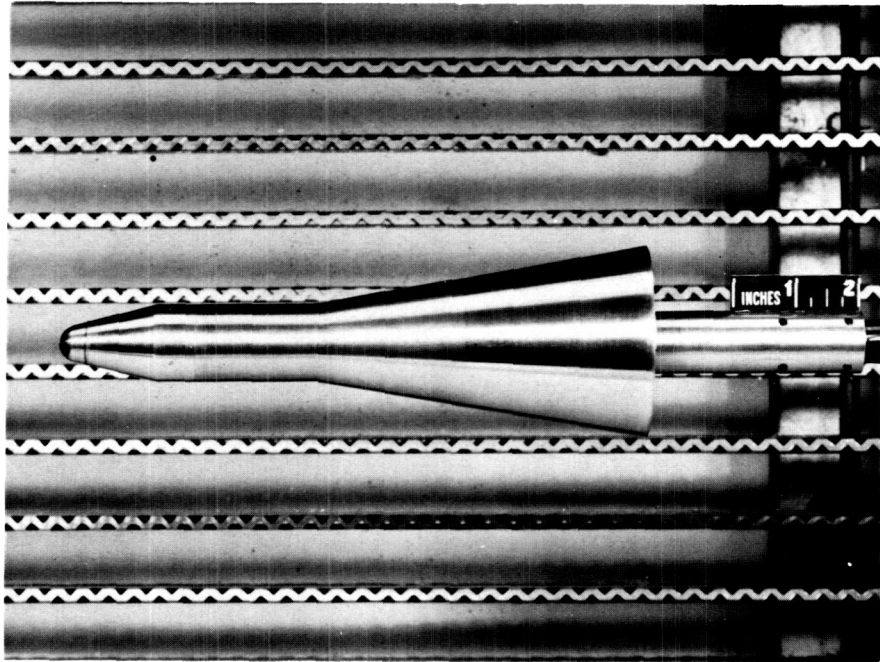
A-24669

(a) Model $N_2B_2F_{10-6}$
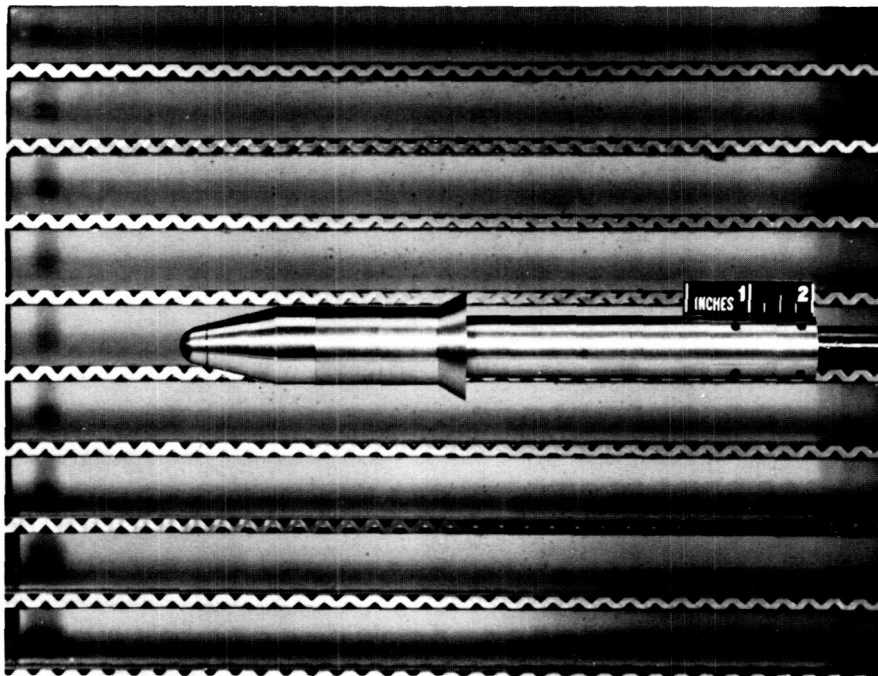
A-24670

(b) Model $N_2B_2F_{30-2}$

Figure 2.- Typical models mounted in the test section.

CONFIDENTIAL

9
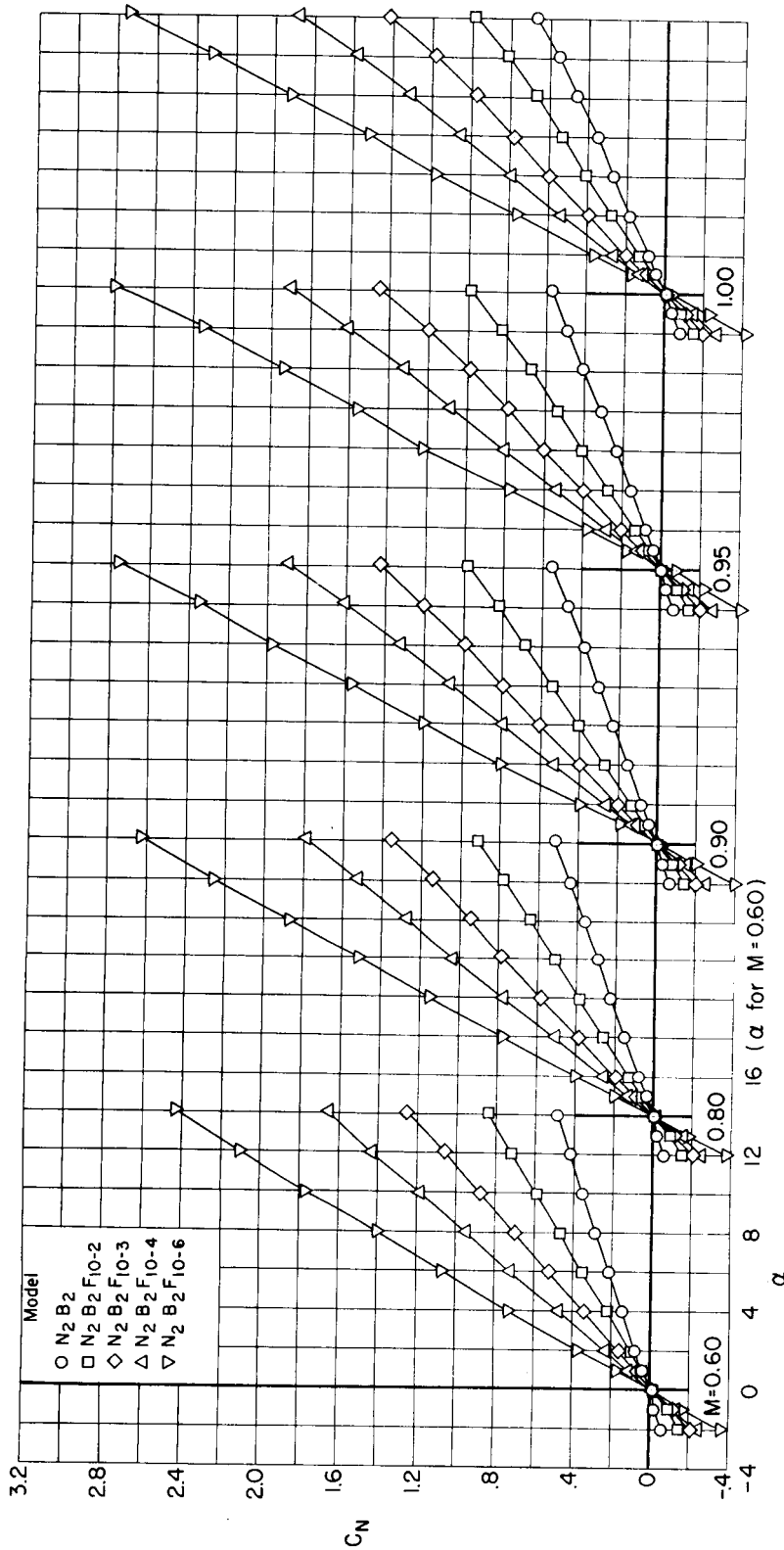
(a) M = 0.60 to 1.00

Figure 3.- Normal-force coefficients for models having 10° flared afterbodies.
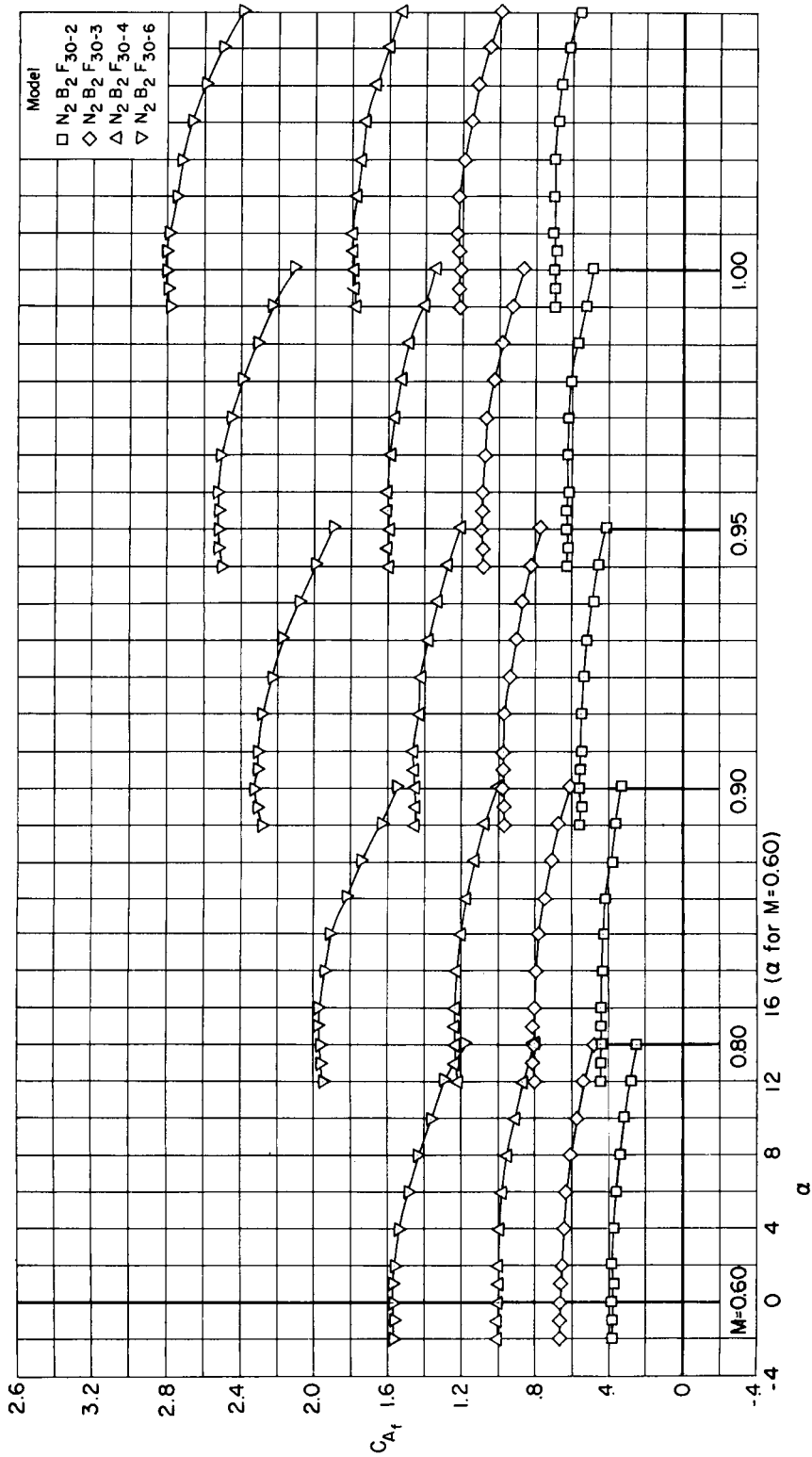
CONFIDENTIAL
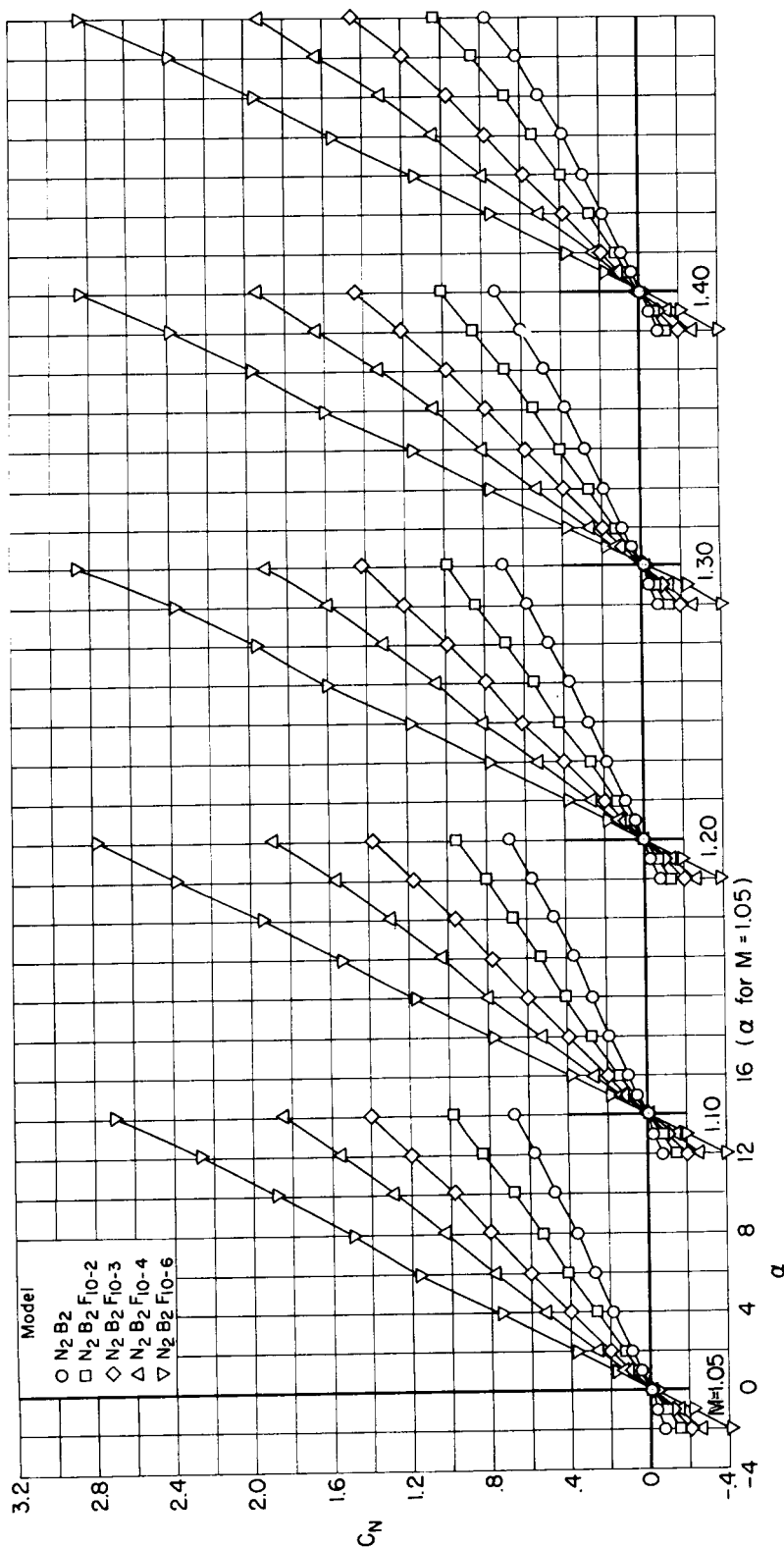
(b) M = 1.05 to 1.40

Figure 3.- Concluded.
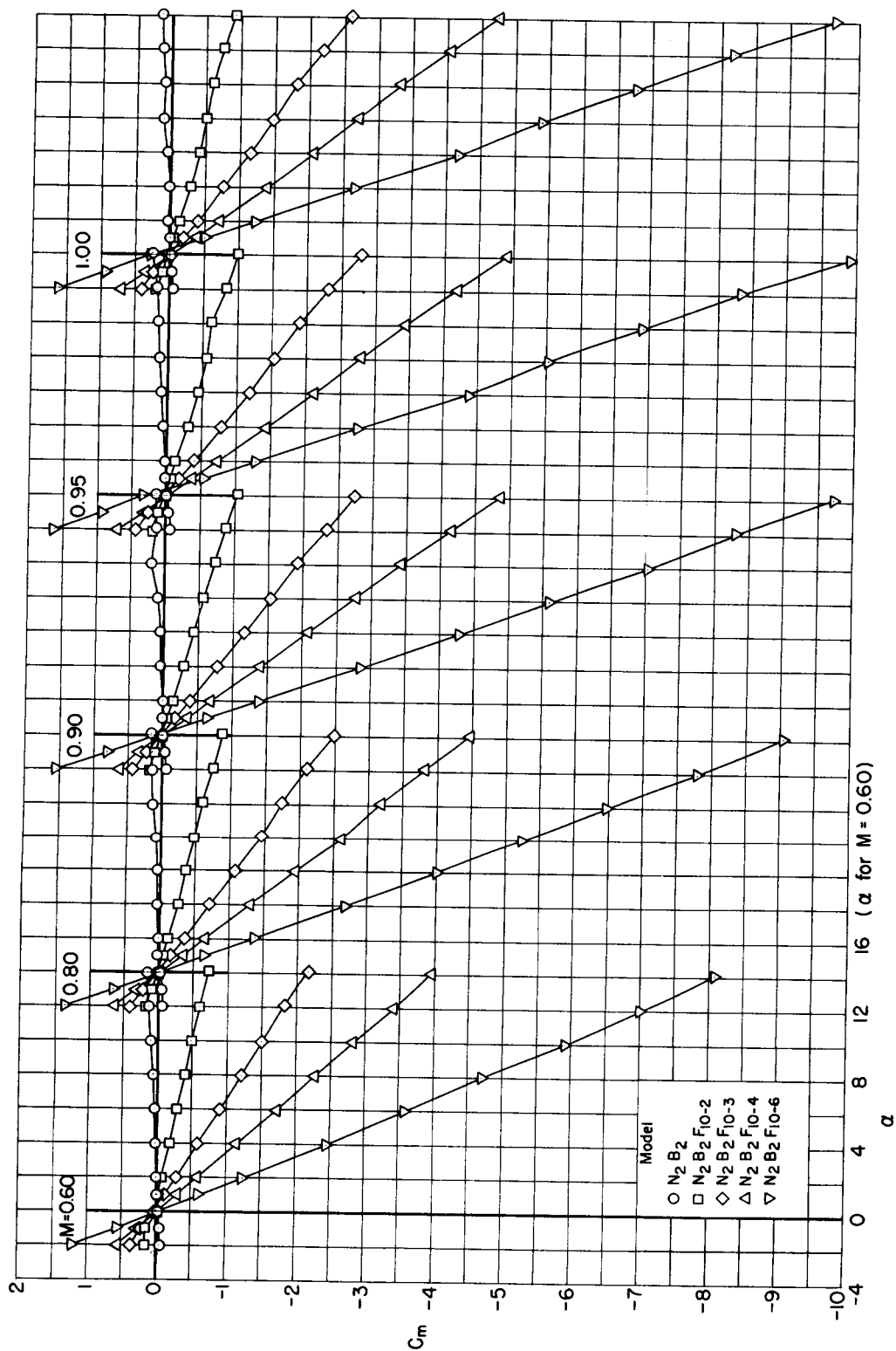
(a) M = 0.60 to 1.00

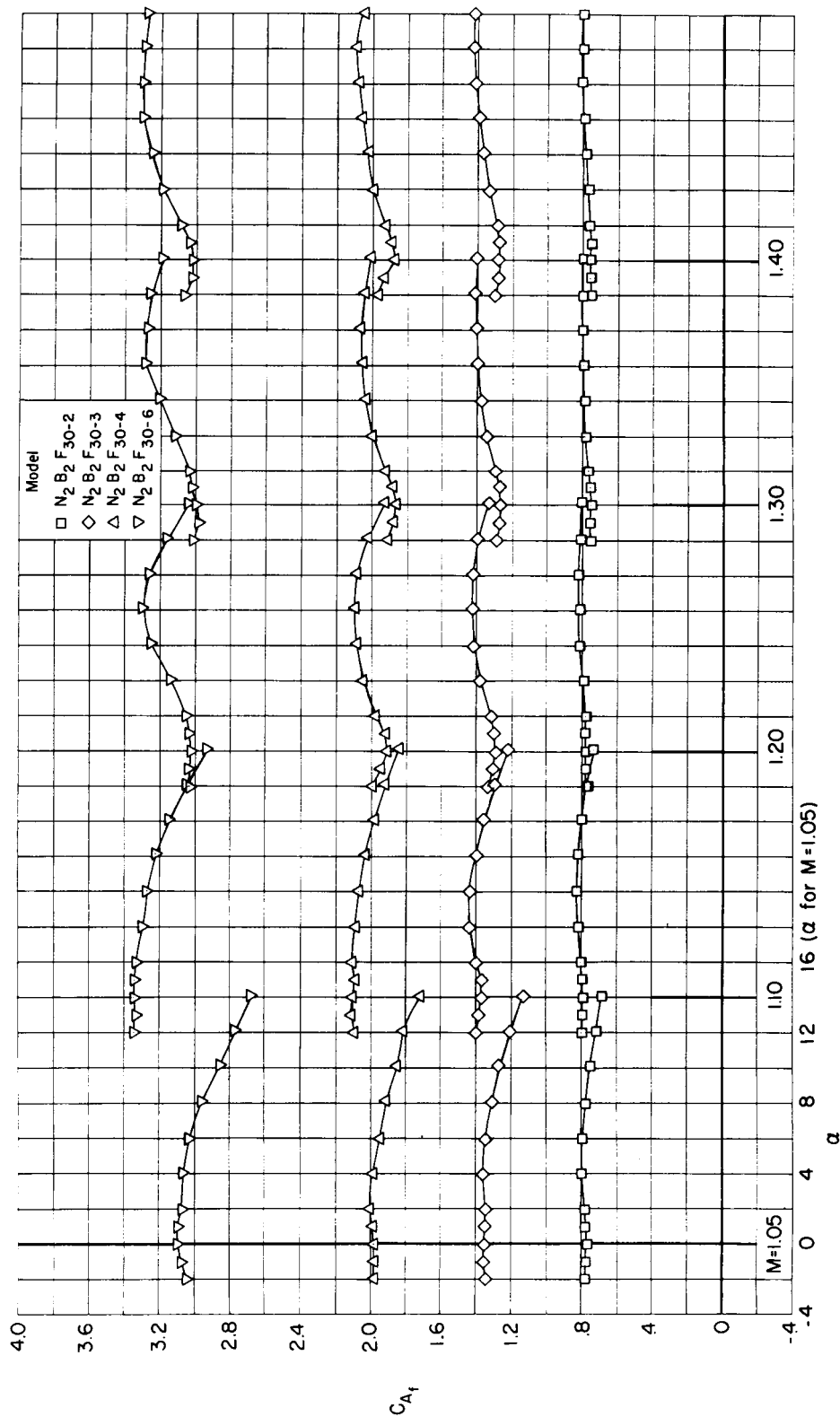Figure 4.- Pitching-moment coefficients for models having 10° flared afterbodies.
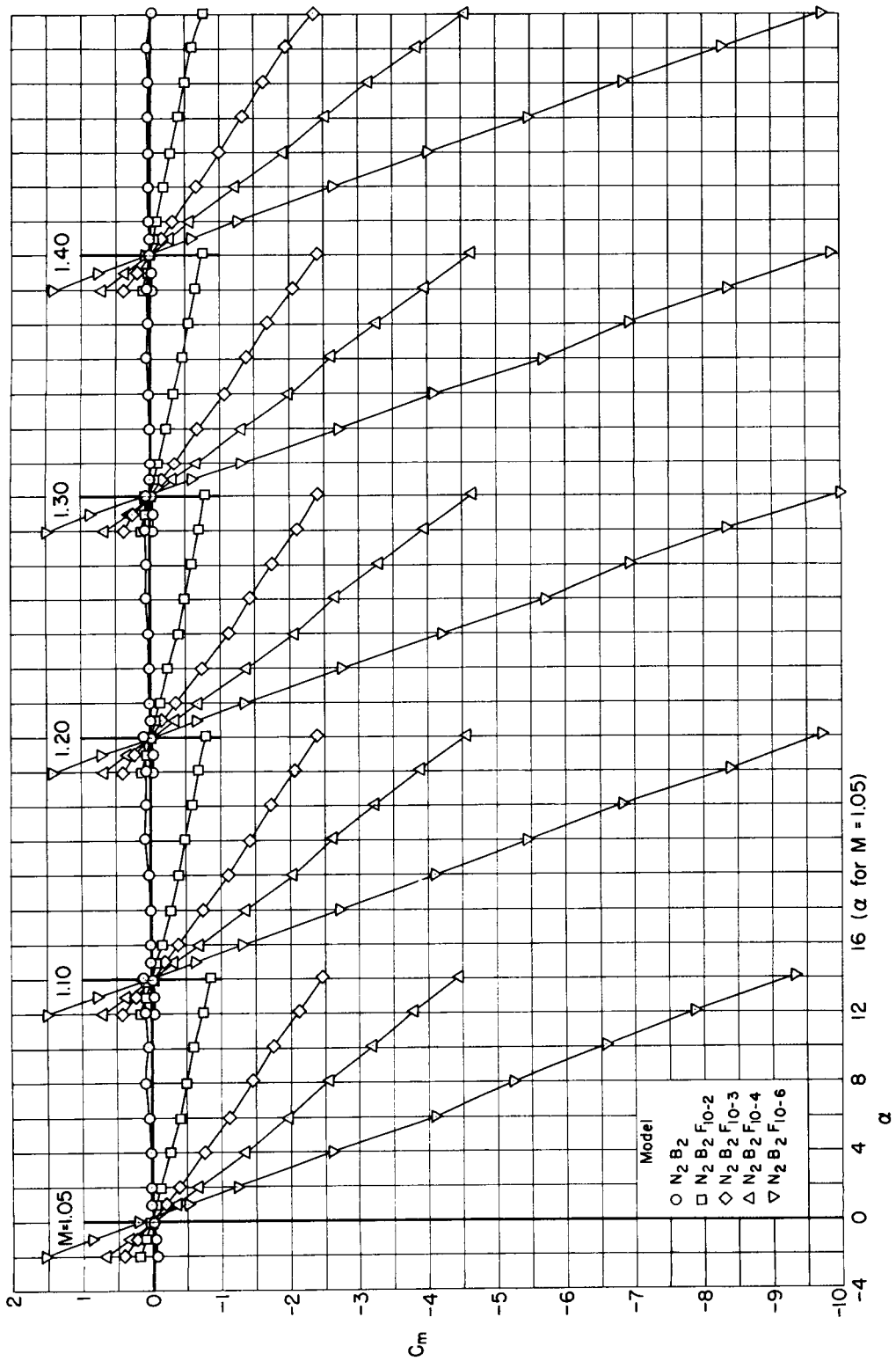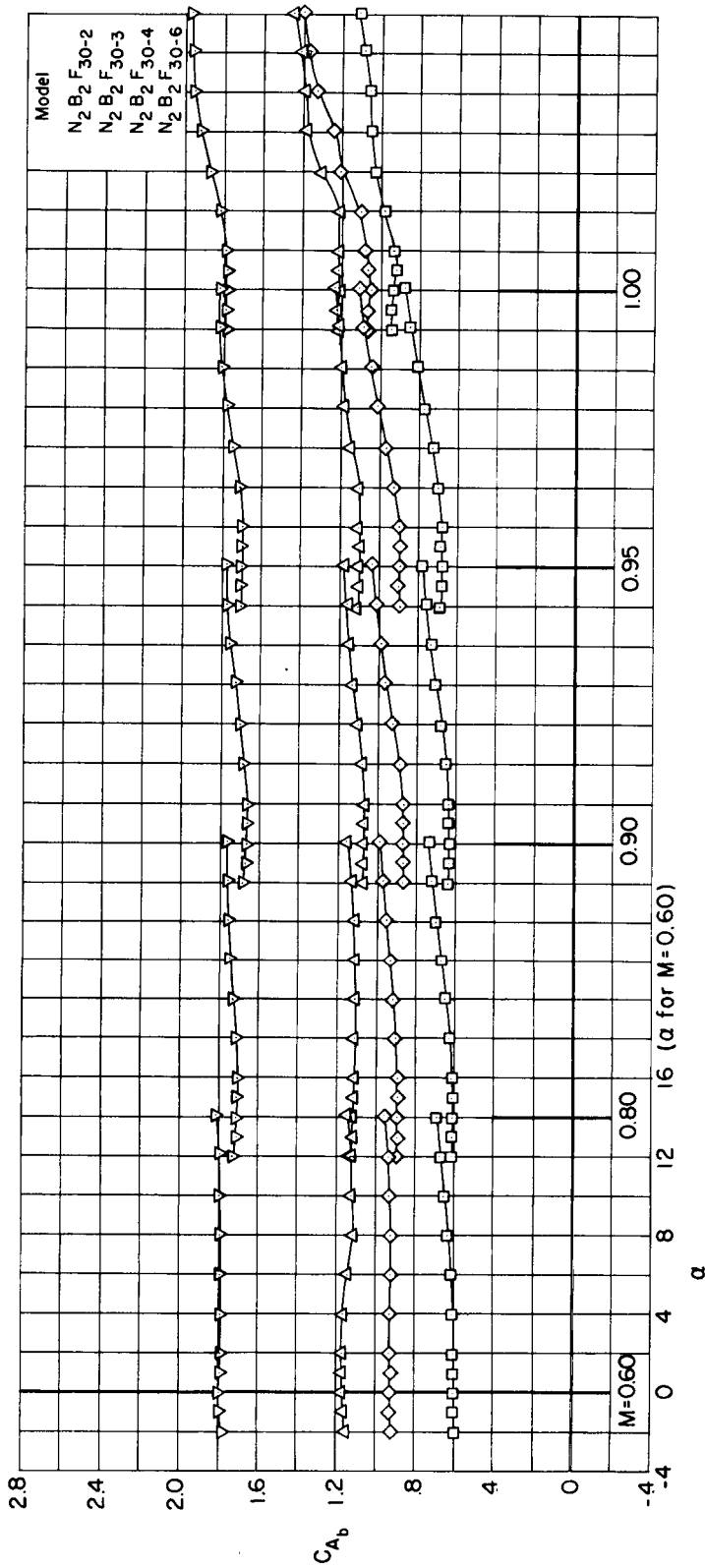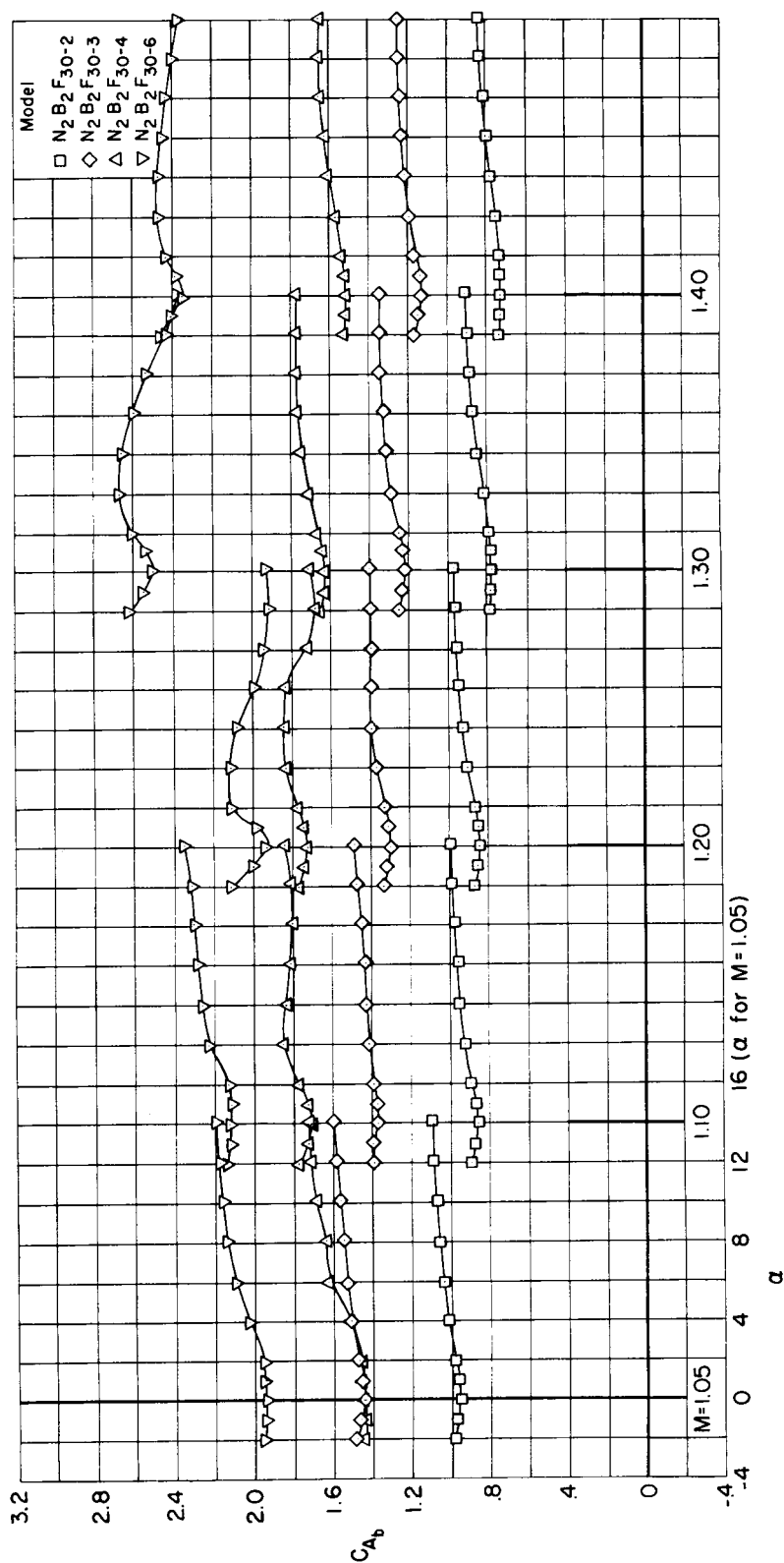
(b) M = 1.05 to 1.40

Figure 4.- Concluded.
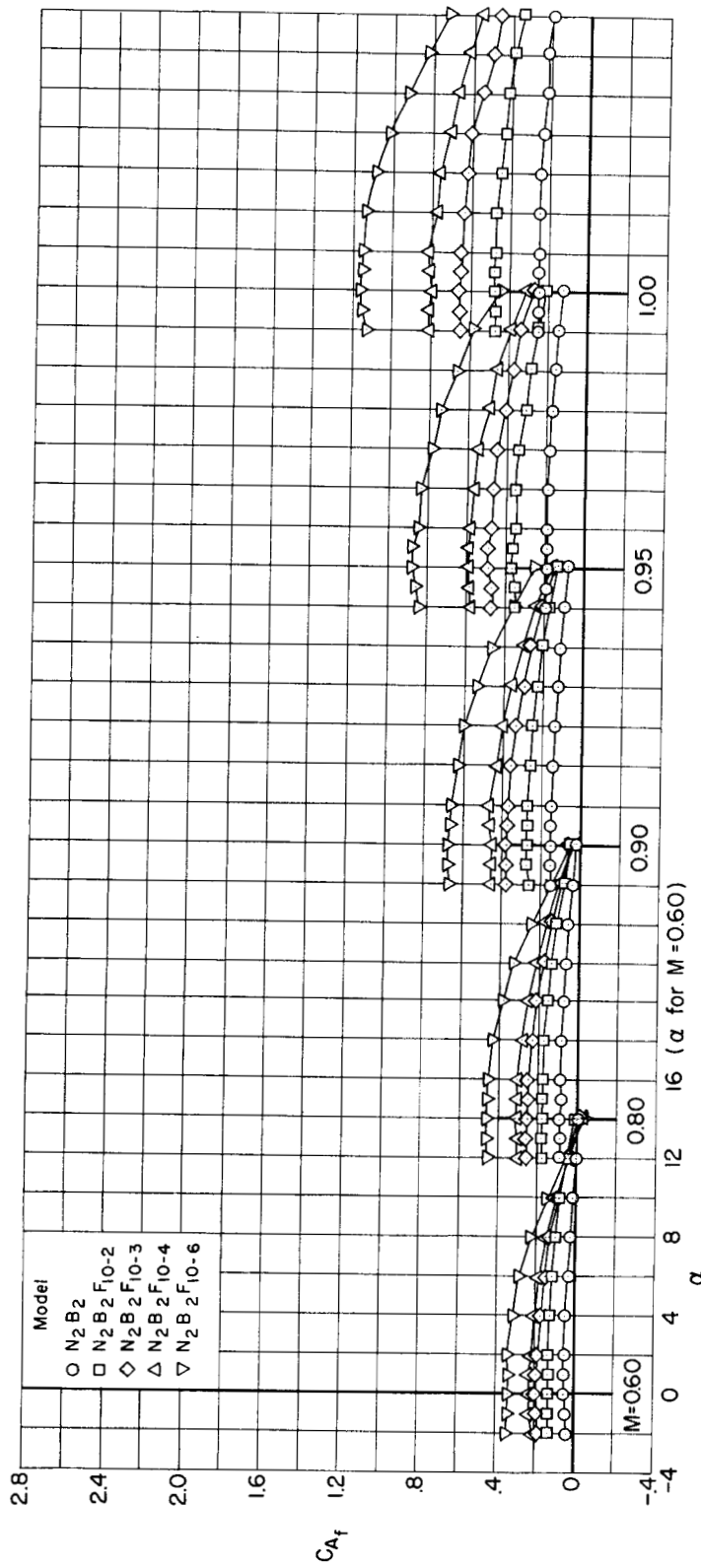
(a) M = 0.60 to 1.00

Figure 5.- Forebody axial-force coefficients for models having 10° flared afterbodies.
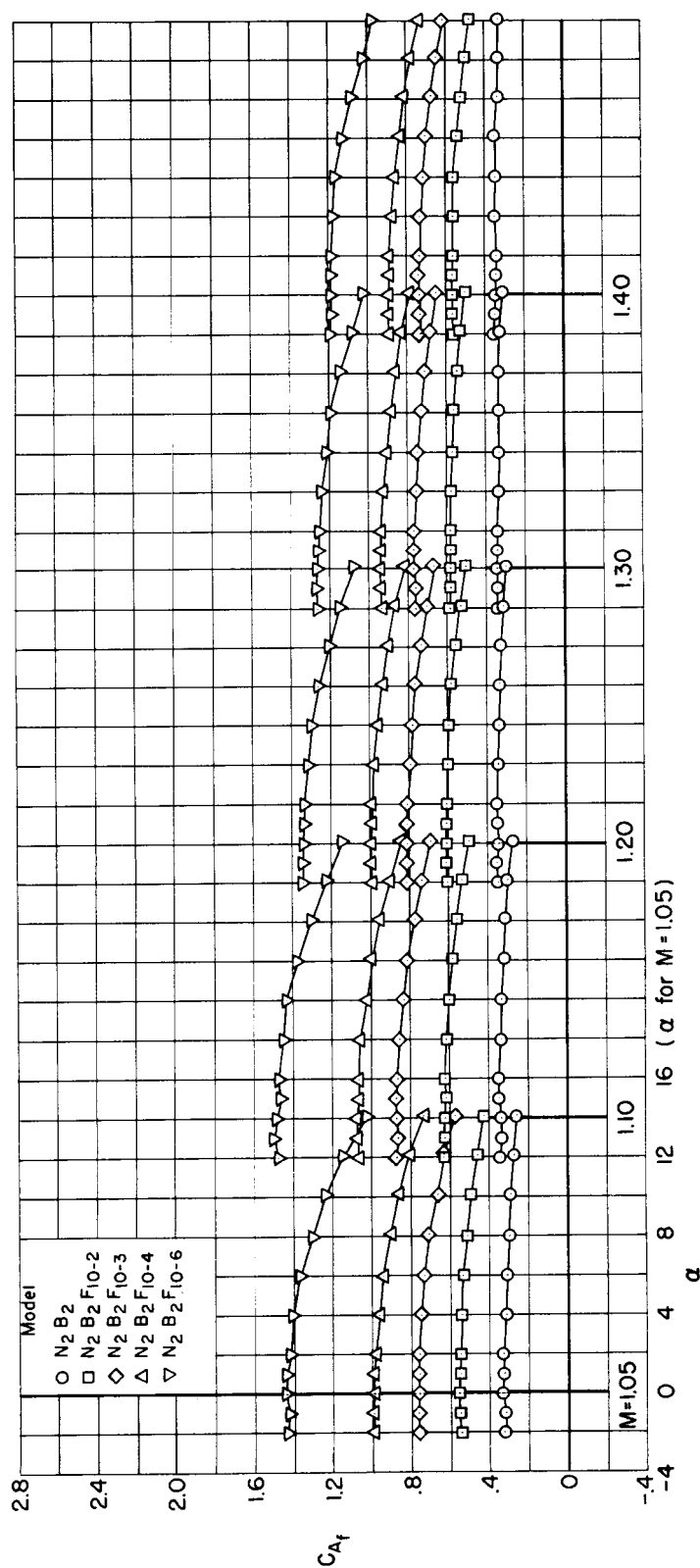
(b) M = 1.05 to 1.40

Figure 5.- Concluded.
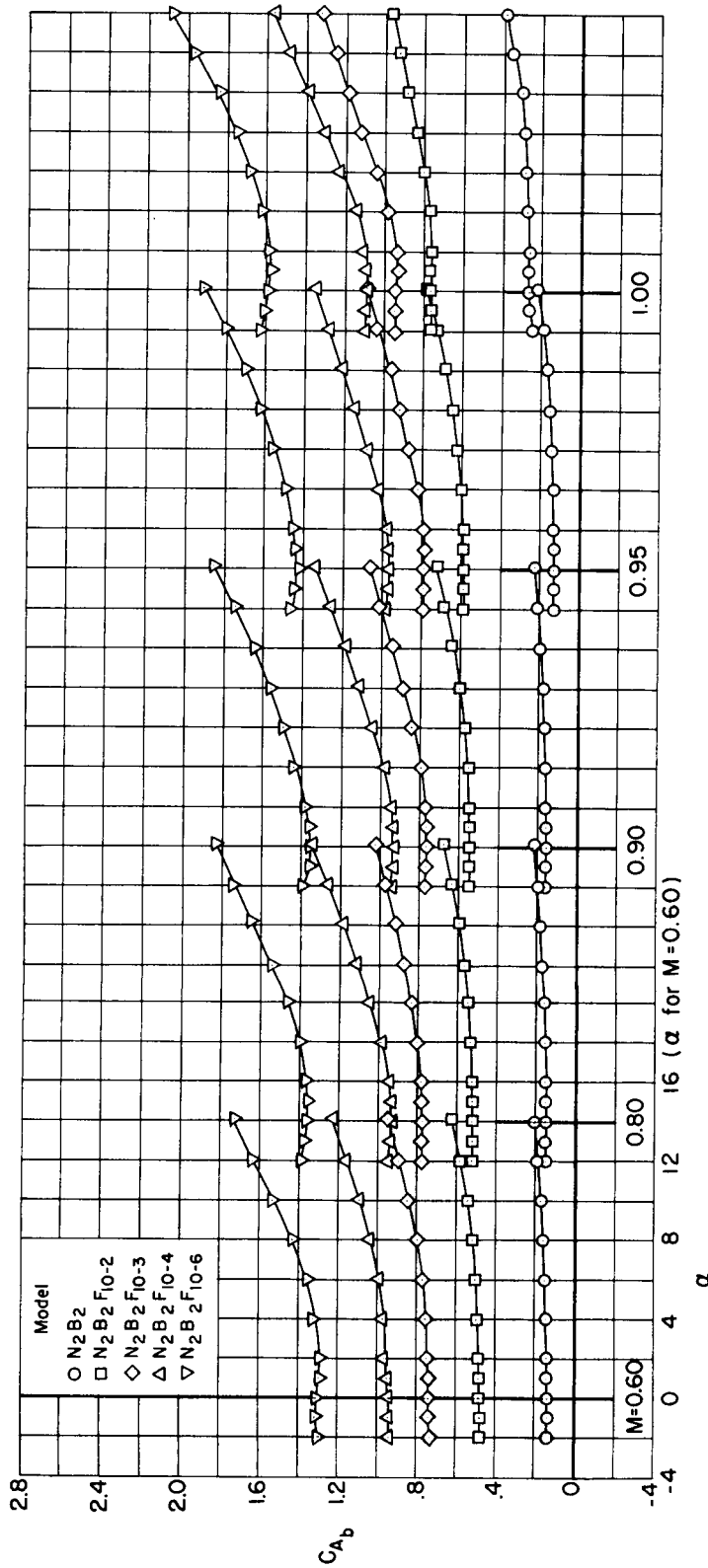
(a) M = 0.60 to 1.00

Figure 6.- Base axial-force coefficients for models having 10° flared afterbodies.
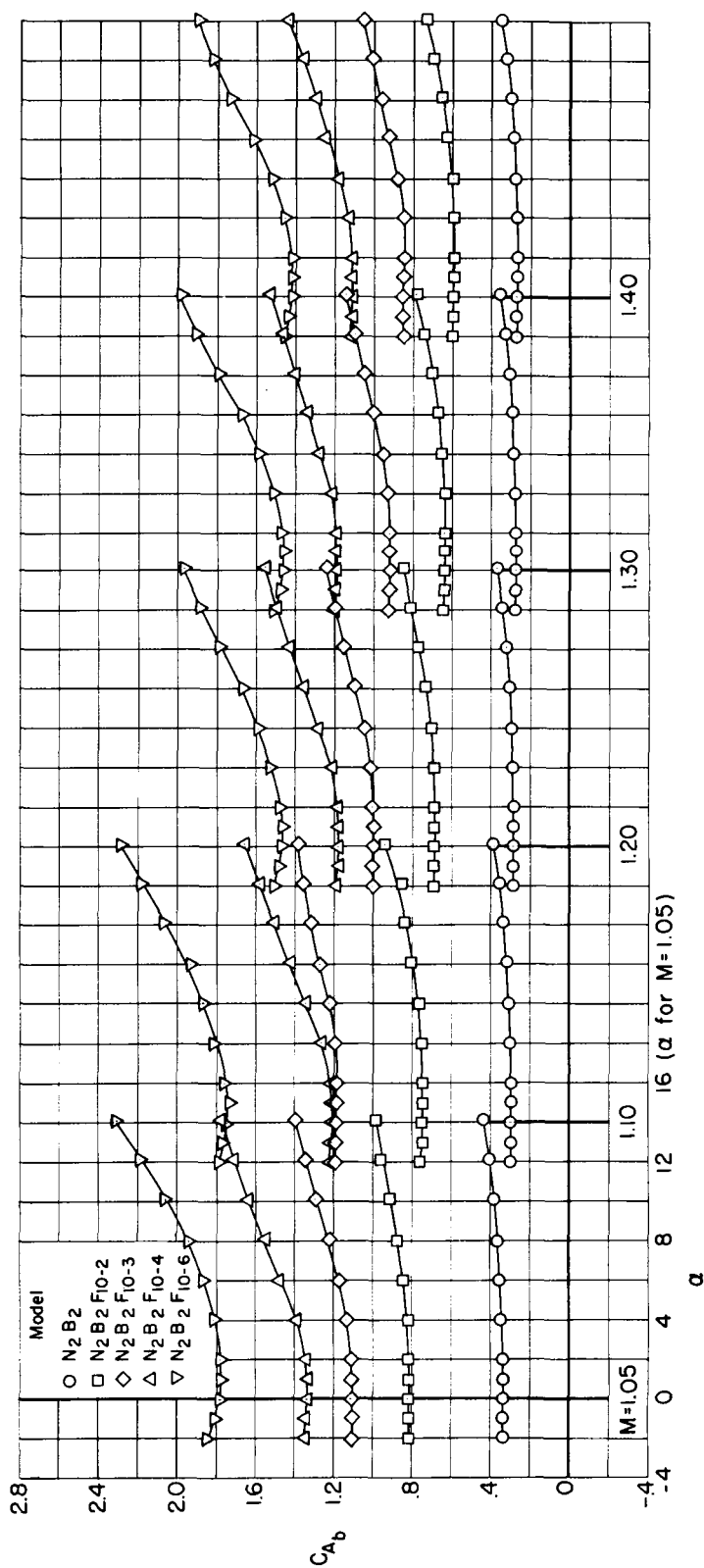
(b) M = 1.05 to 1.40

Figure 6.- Concluded.
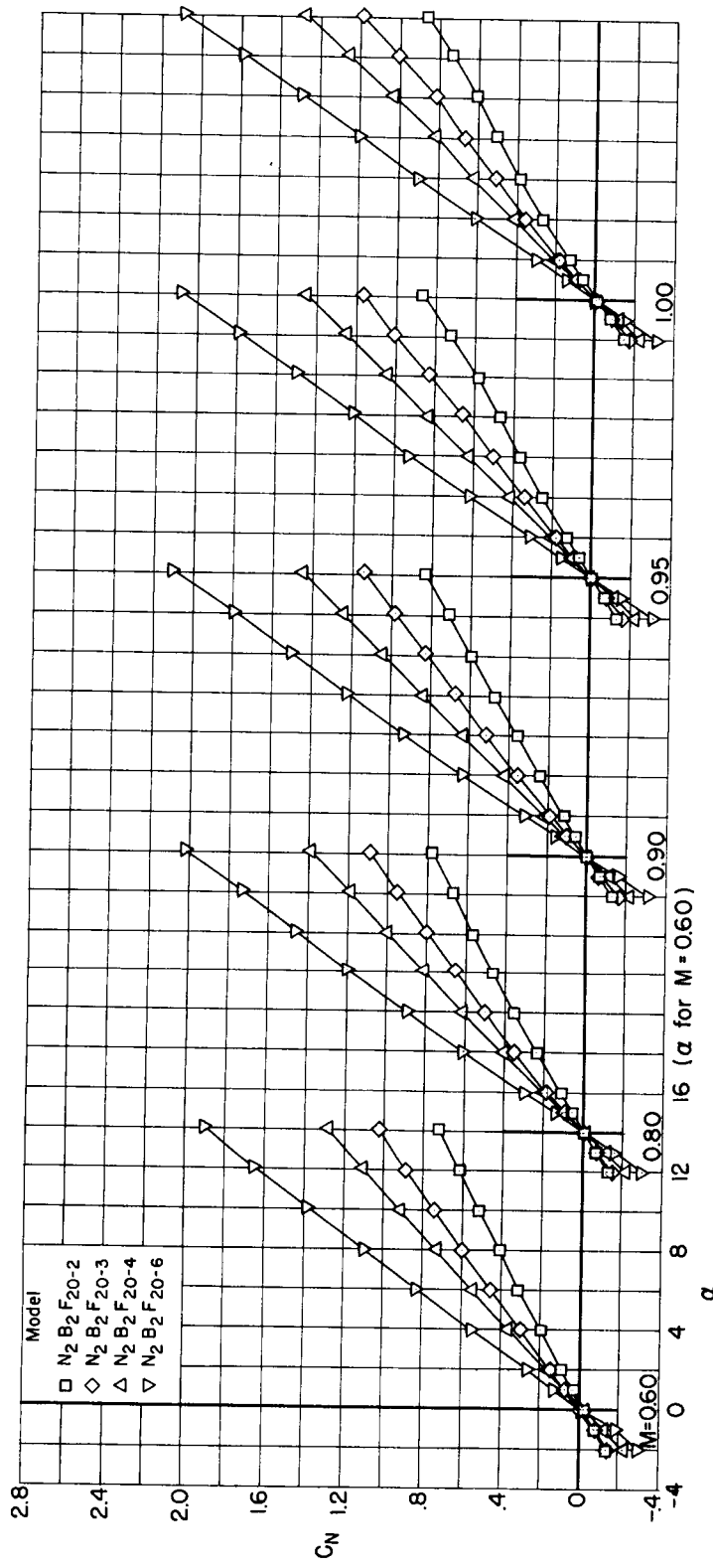
(a) M = 0.60 to 1.00

Figure 7.- Normal-force coefficients for models having 20° flared afterbodies.
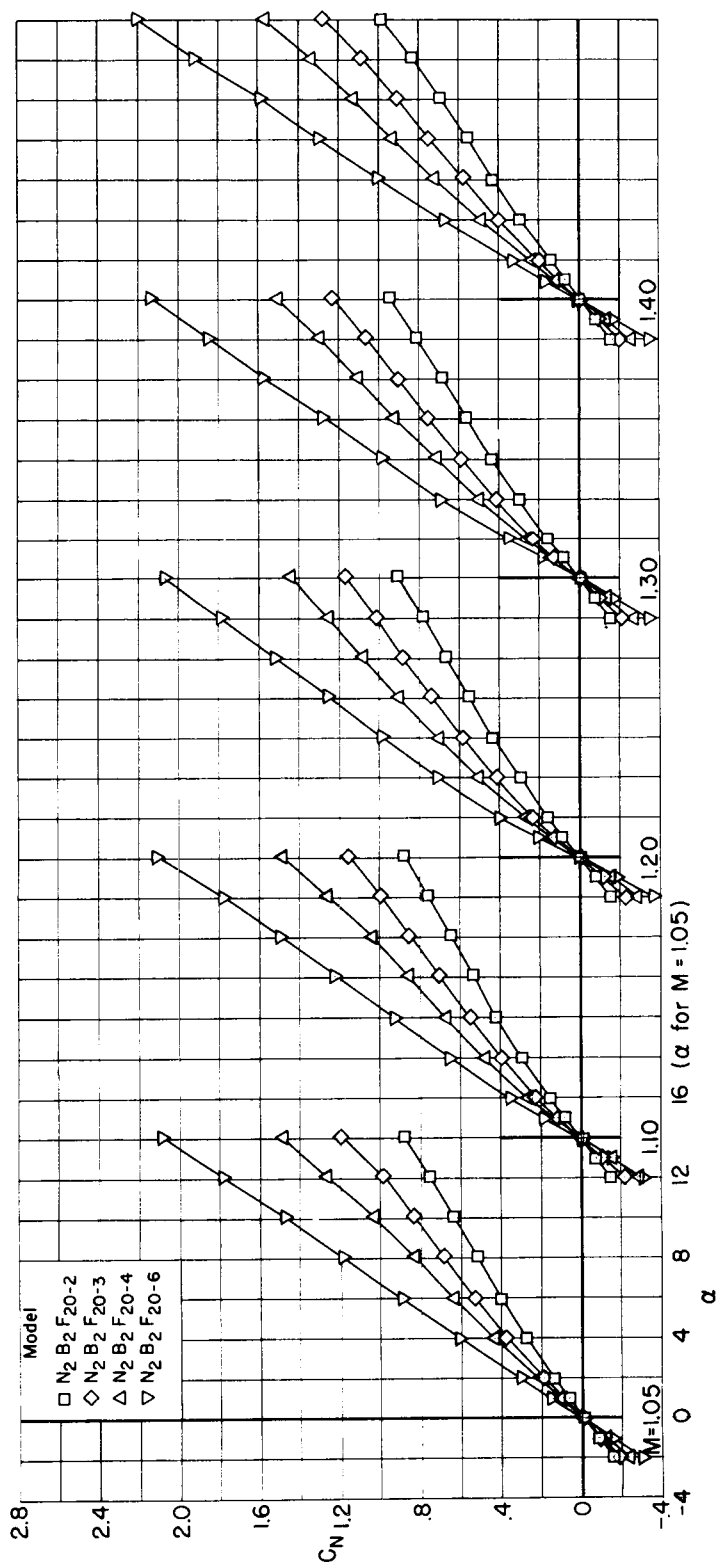
(b) M = 1.05 to 1.40

Figure 7.- Concluded.
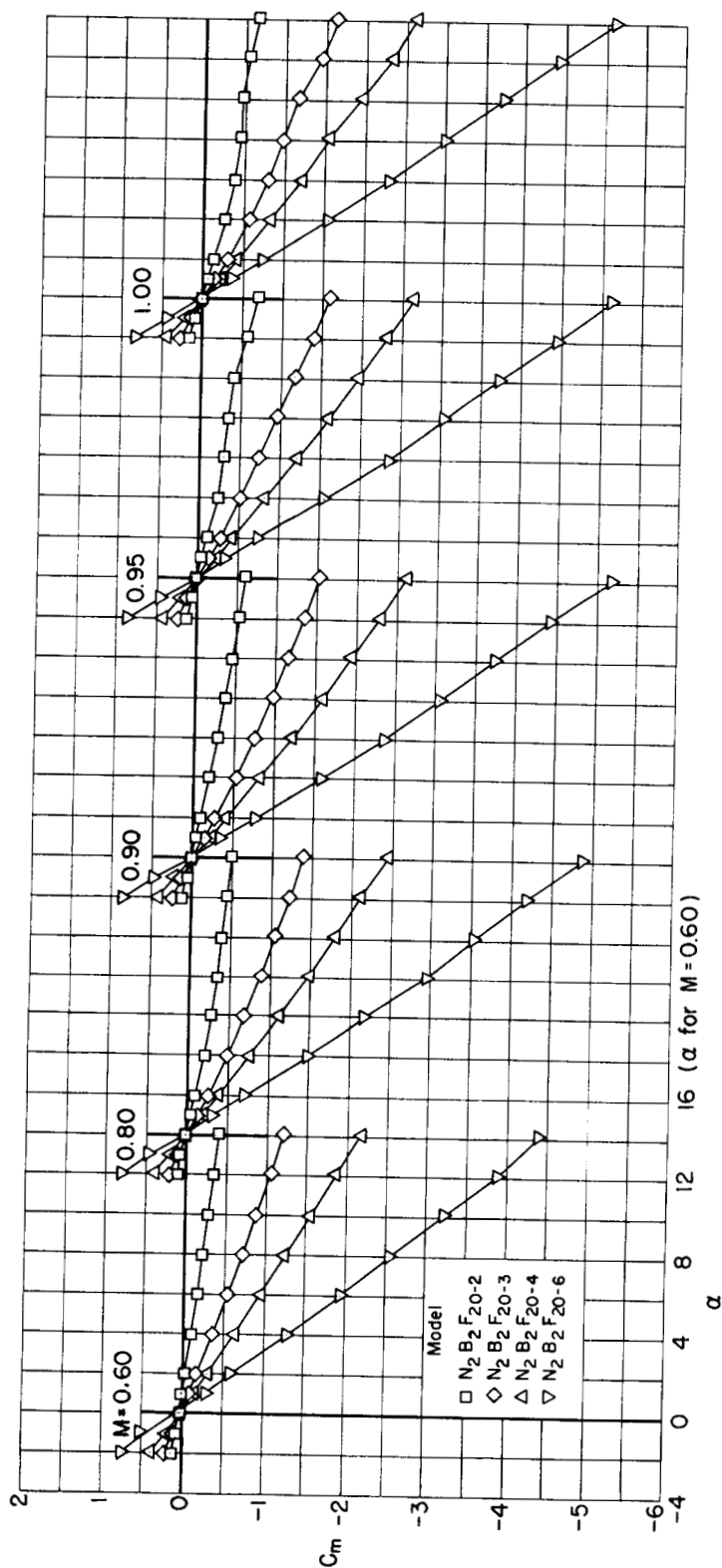
(a) M = 0.60 to 1.00

Figure 8.- Pitching-moment coefficients for models having 20° flared afterbodies.
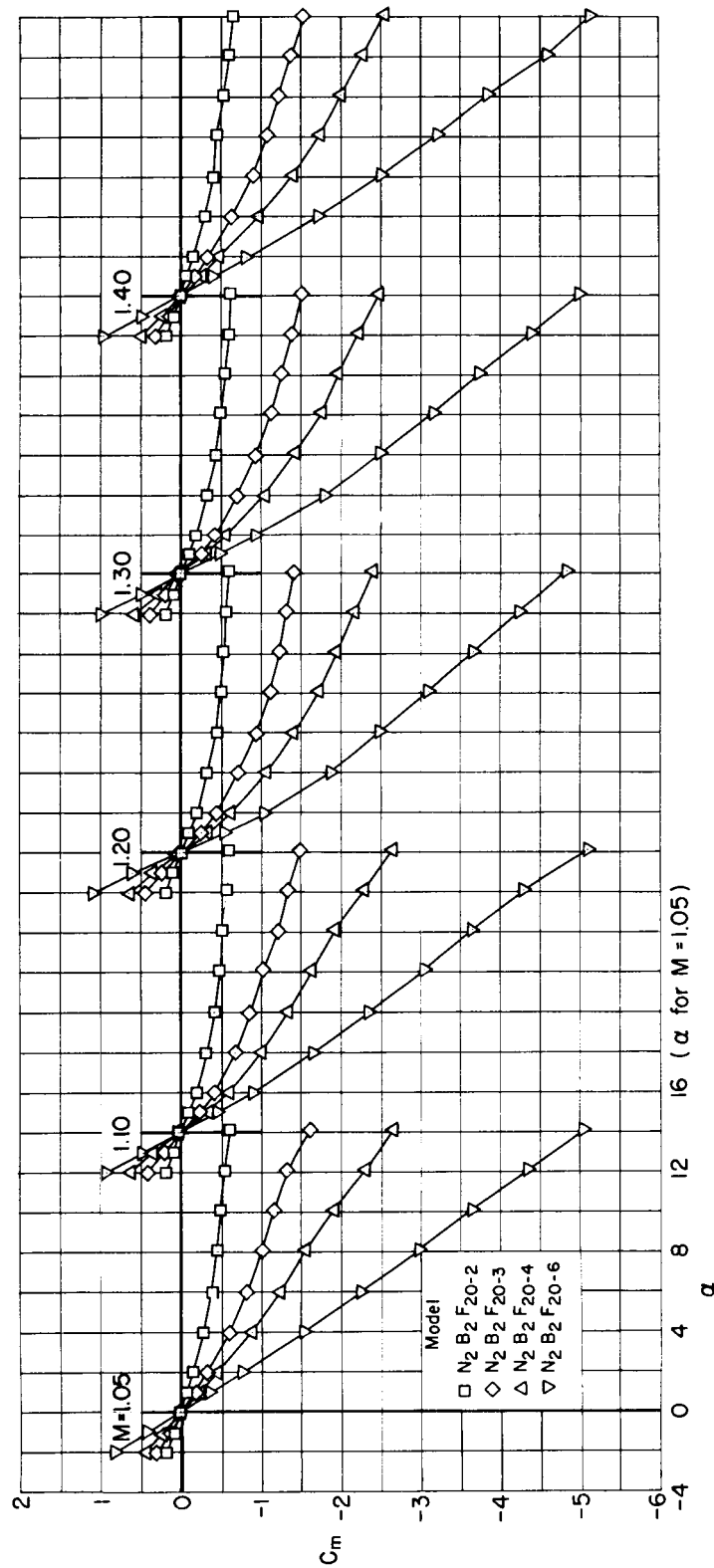
(b) M = 1.05 to 1.40

Figure 8.- Concluded.
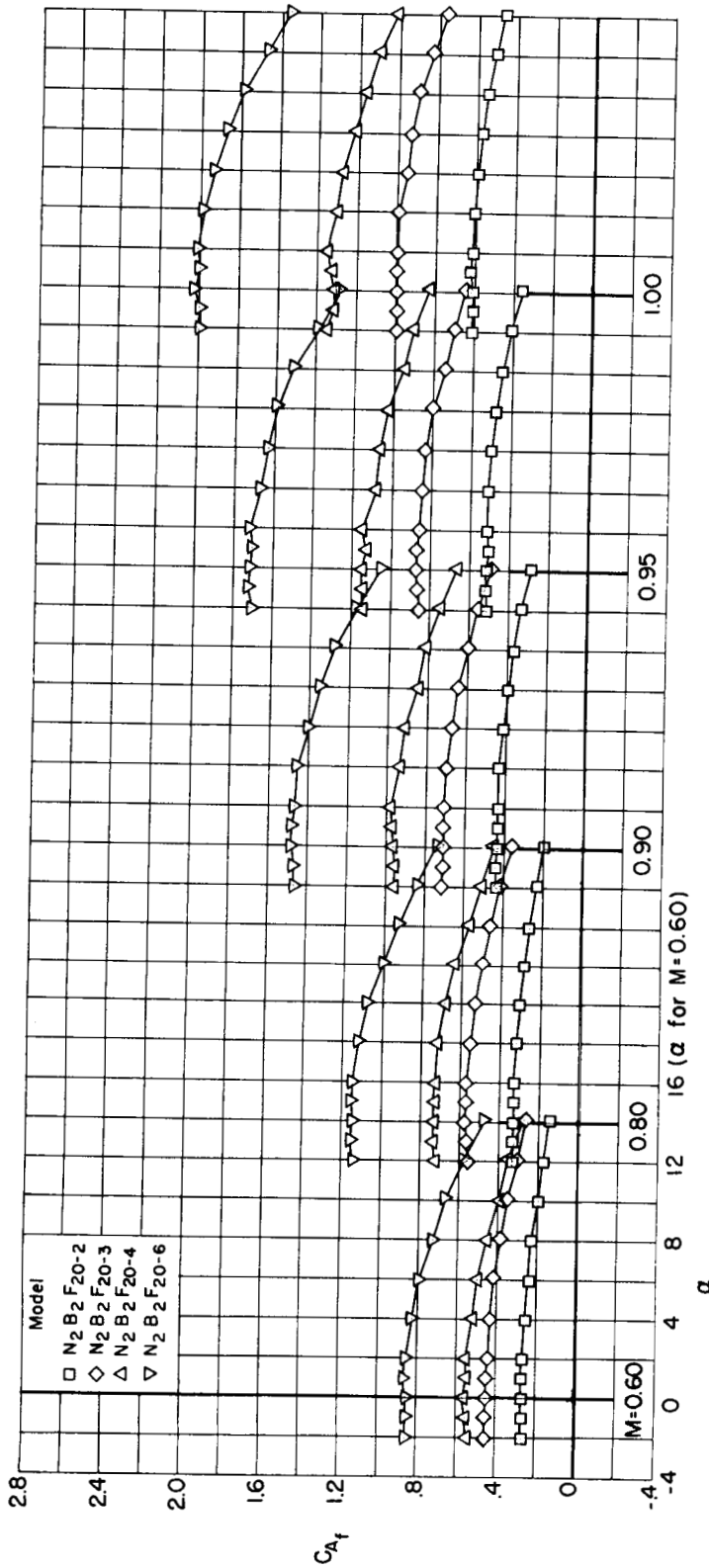
(a) M = 0.60 to 1.00

Figure 9.- Forebody axial-force coefficients for models having 20° flared afterbodies.
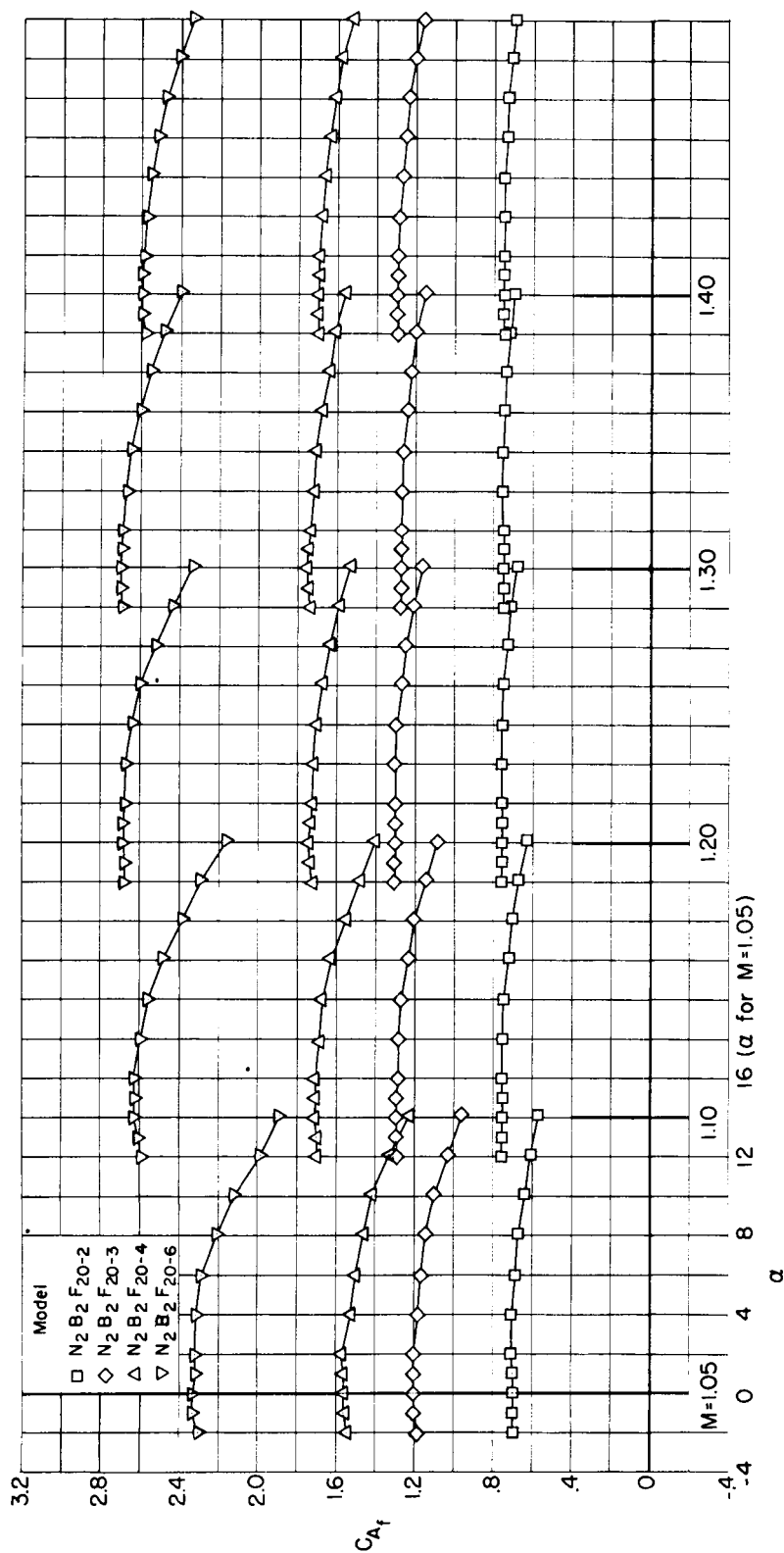
(b) M = 1.05 to 1.40

Figure 9.- Concluded.
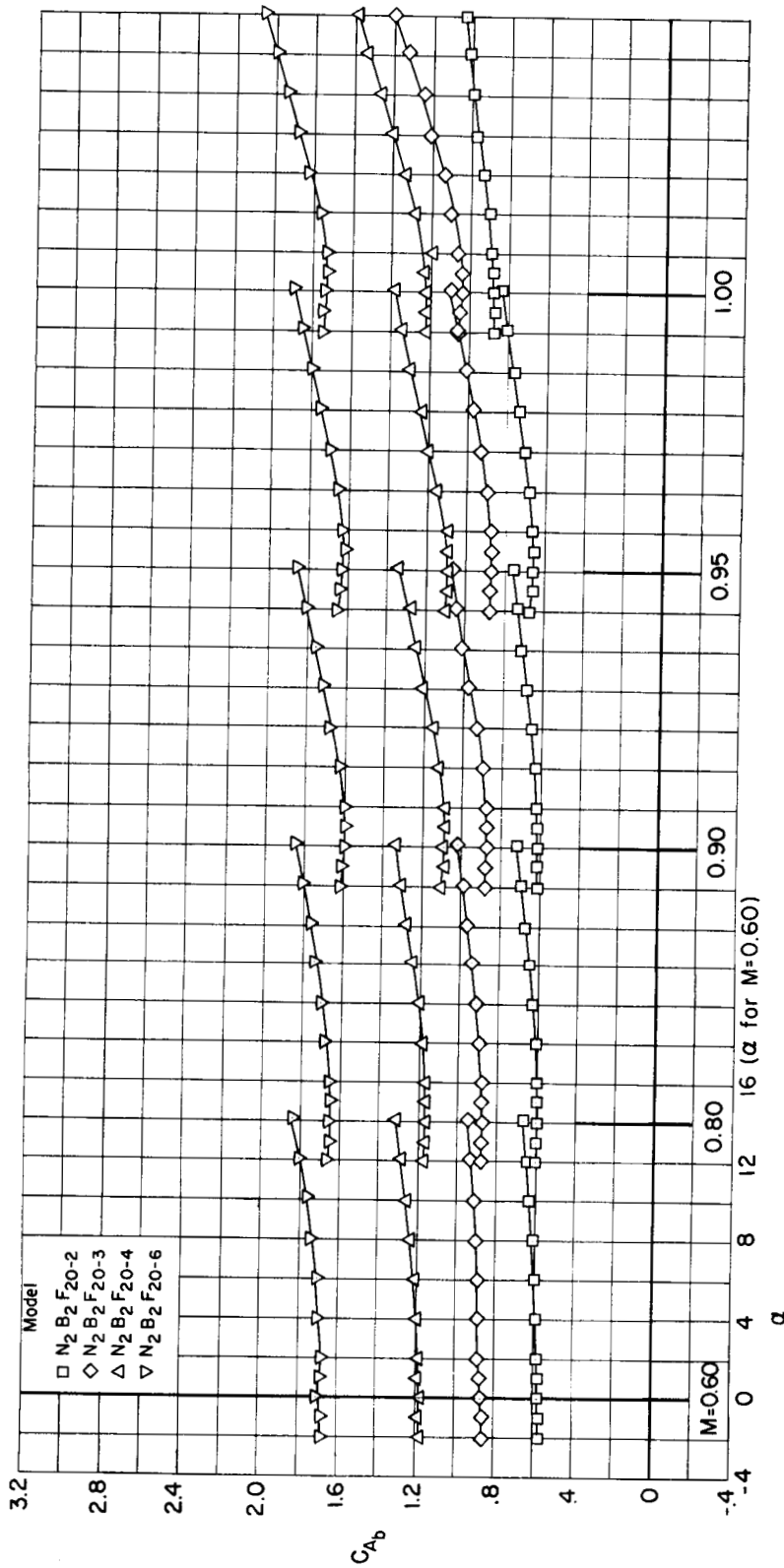
(a) M = 0.60 to 1.00

Figure 10.- Base axial-force coefficients for models having 20° flared afterbodies.
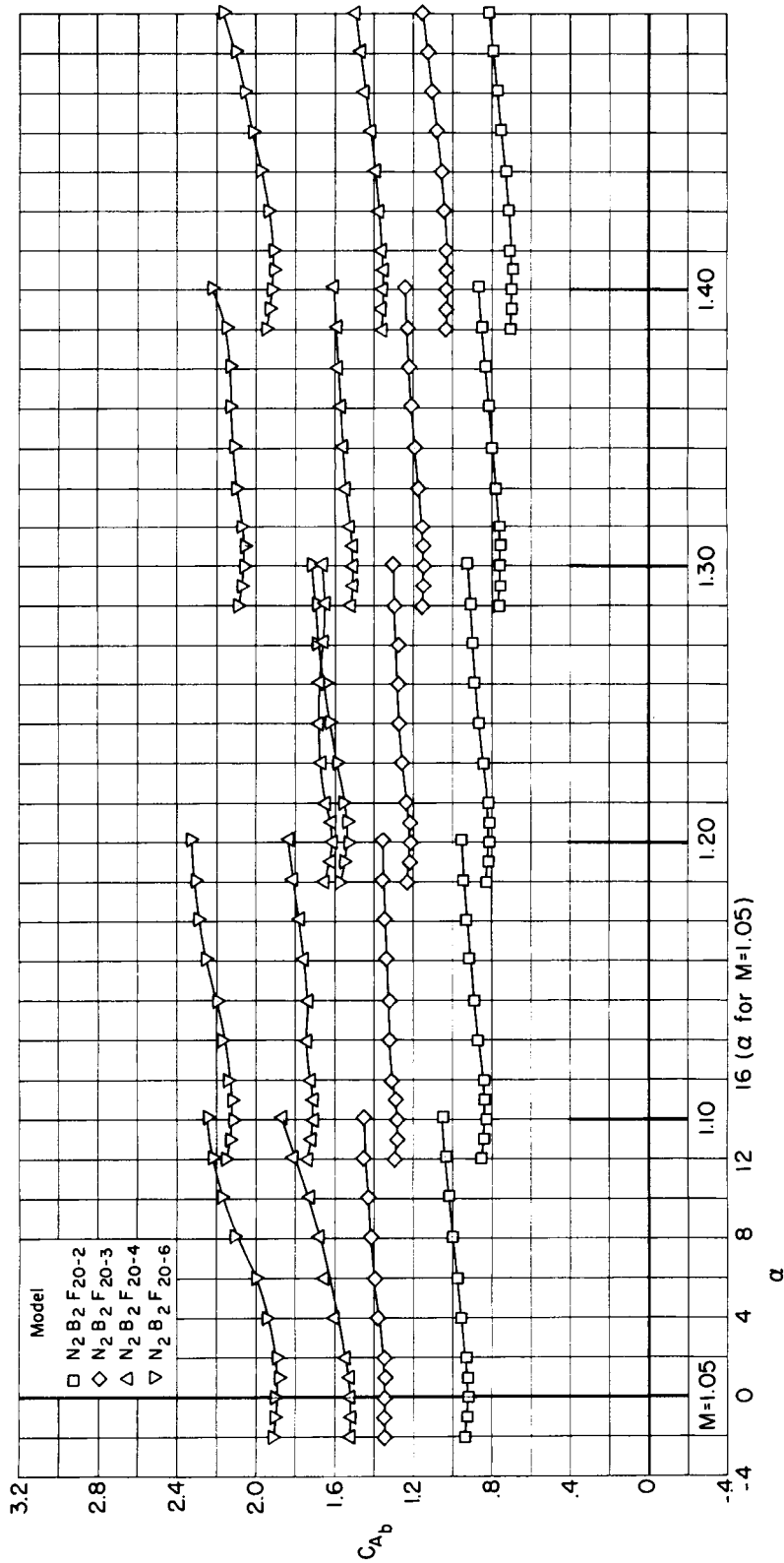
(b) M = 1.05 to 1.40

Figure 10.- Concluded.
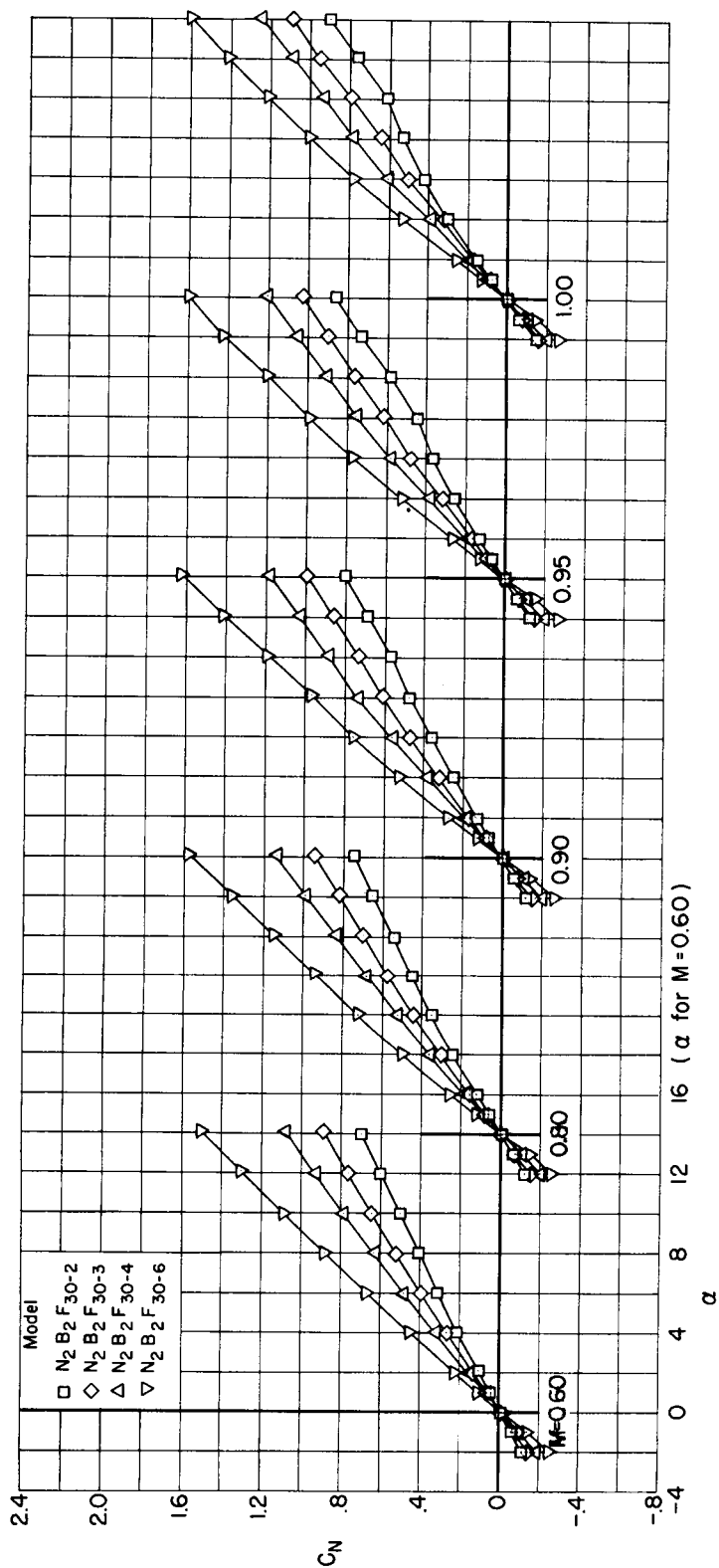
(a) M = 0.60 to 1.00

Figure 11.- Normal-force coefficients for models having 30° flared afterbodies.
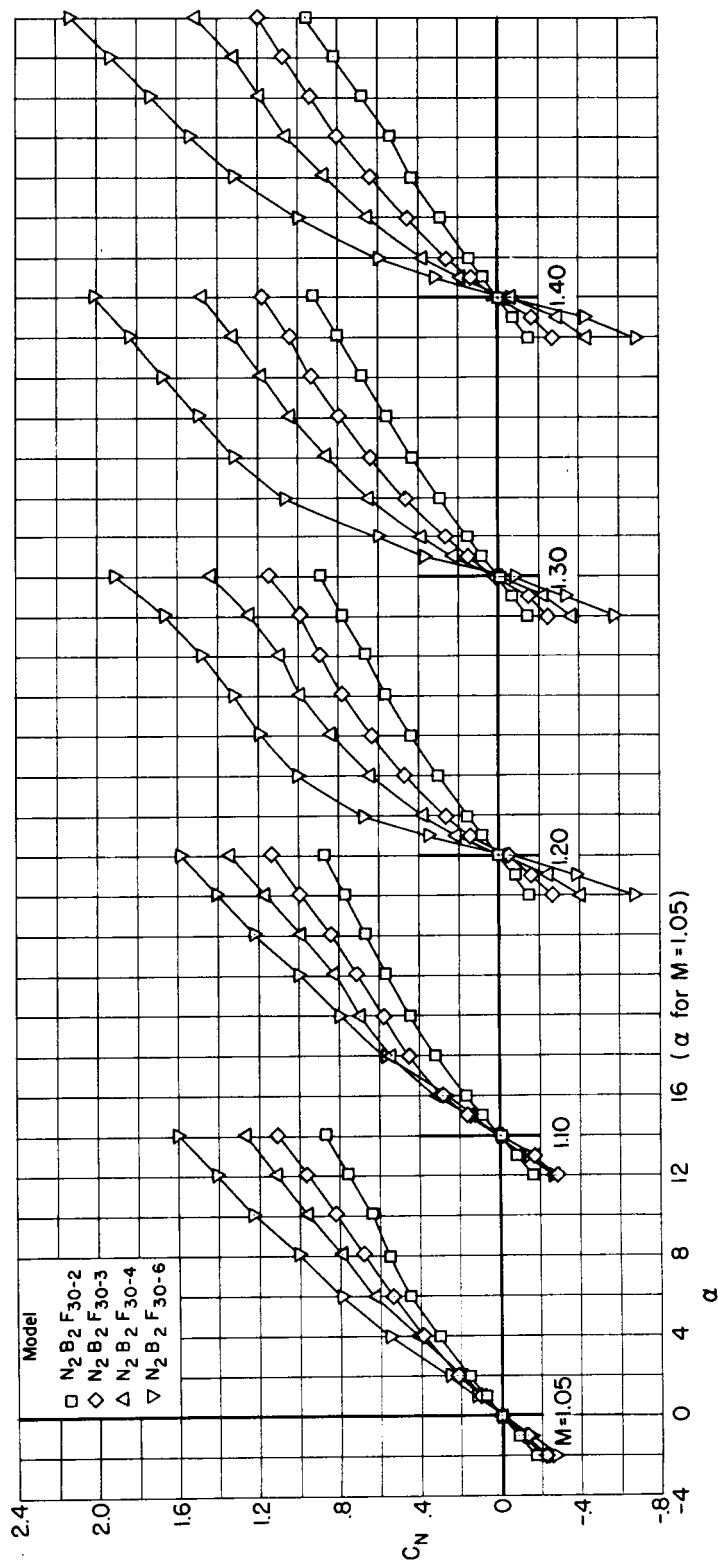
(b) M = 1.05 to 1.40

Figure 11.- Concluded.
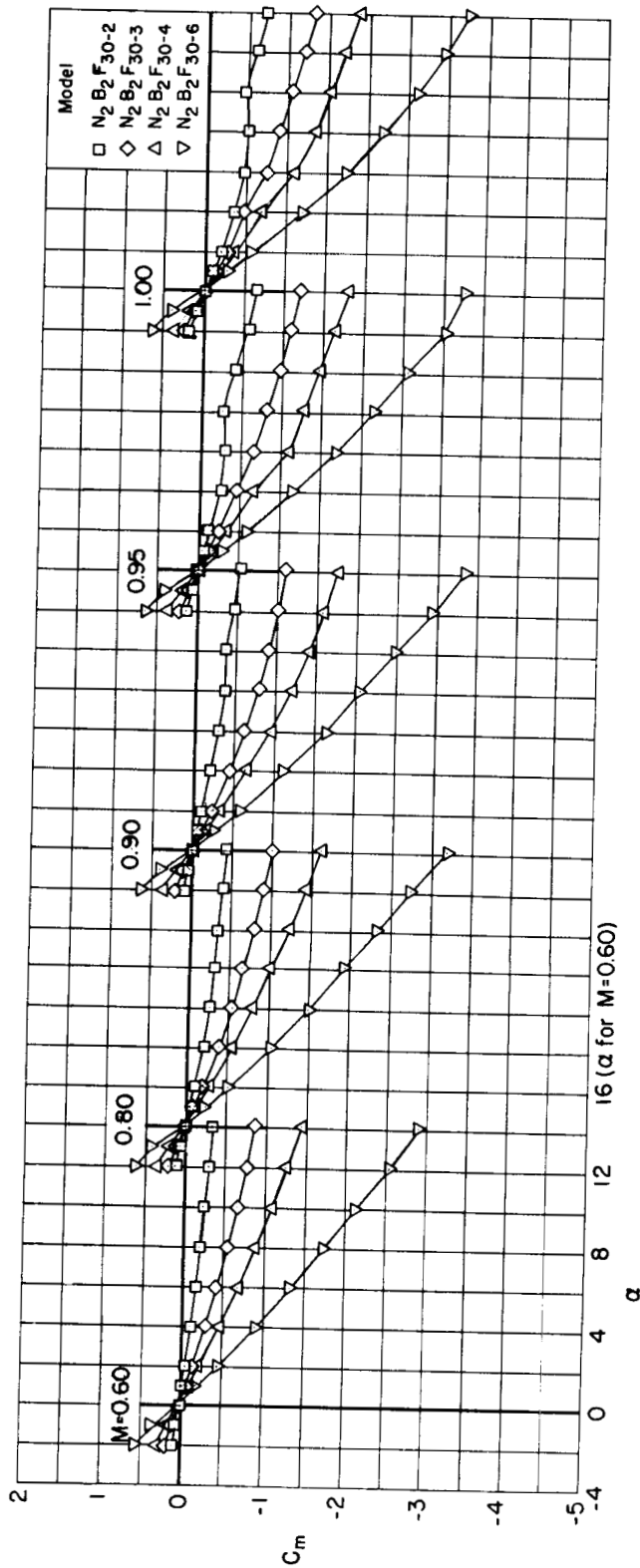
(a) M = 0.60 to 1.00

Figure 12.- Pitching-moment coefficients for models having 30° flared afterbodies.
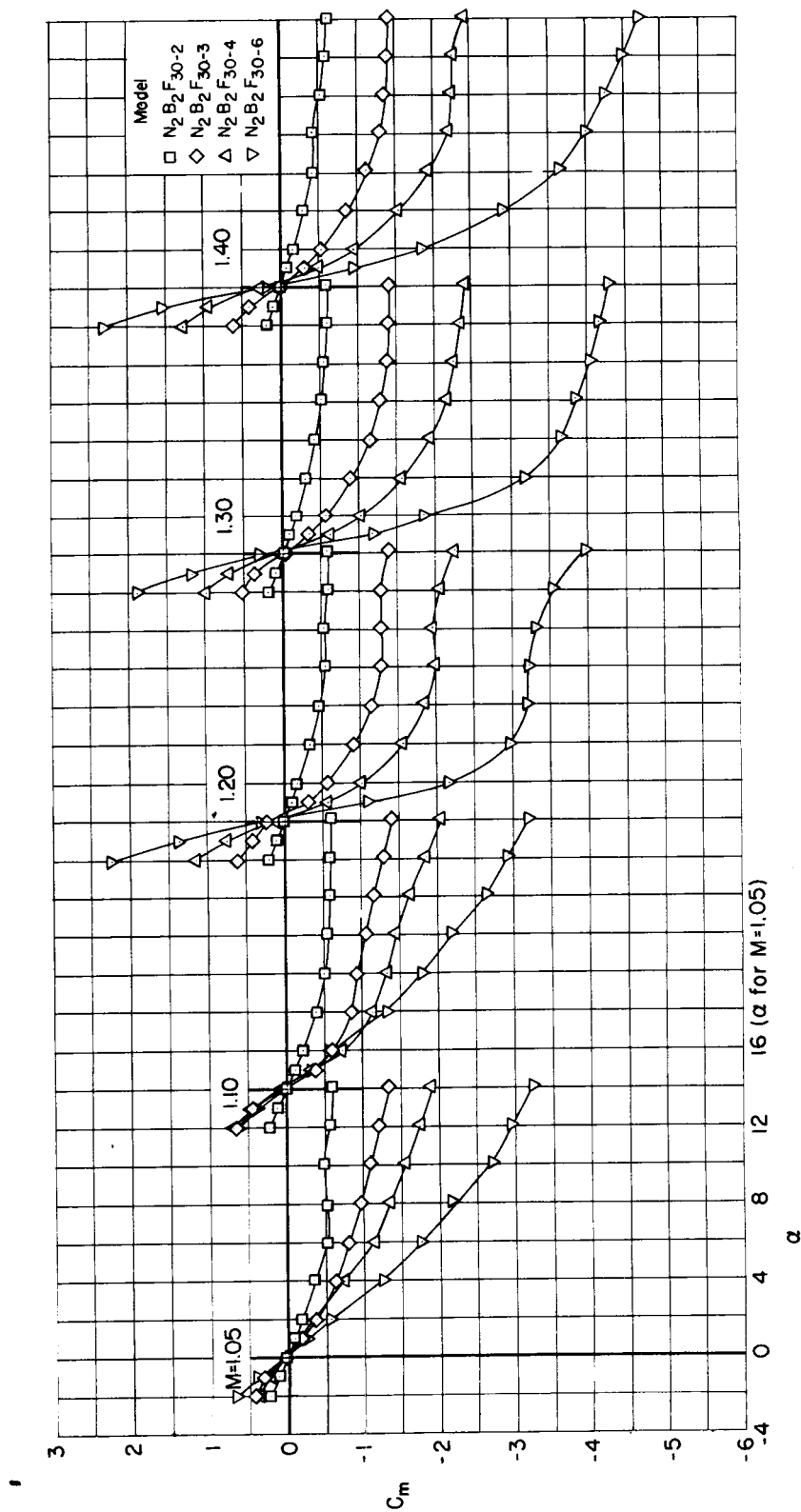
(b) M = 1.05 to 1.40

Figure 12.- Concluded.

(a) M = 0.60 to 1.00

Figure 13.- Forebody axial-force coefficients for models having $30°$ flared afterbodies.

(b) M = 1.05 to 1.40

Figure 13.- Concluded.

(a) M = 0.60 to 1.00

Figure 14.- Base axial-force coefficients for models having 30° flared afterbodies.

(b) M = 1.05 to 1.40

Figure 14.- Concluded.
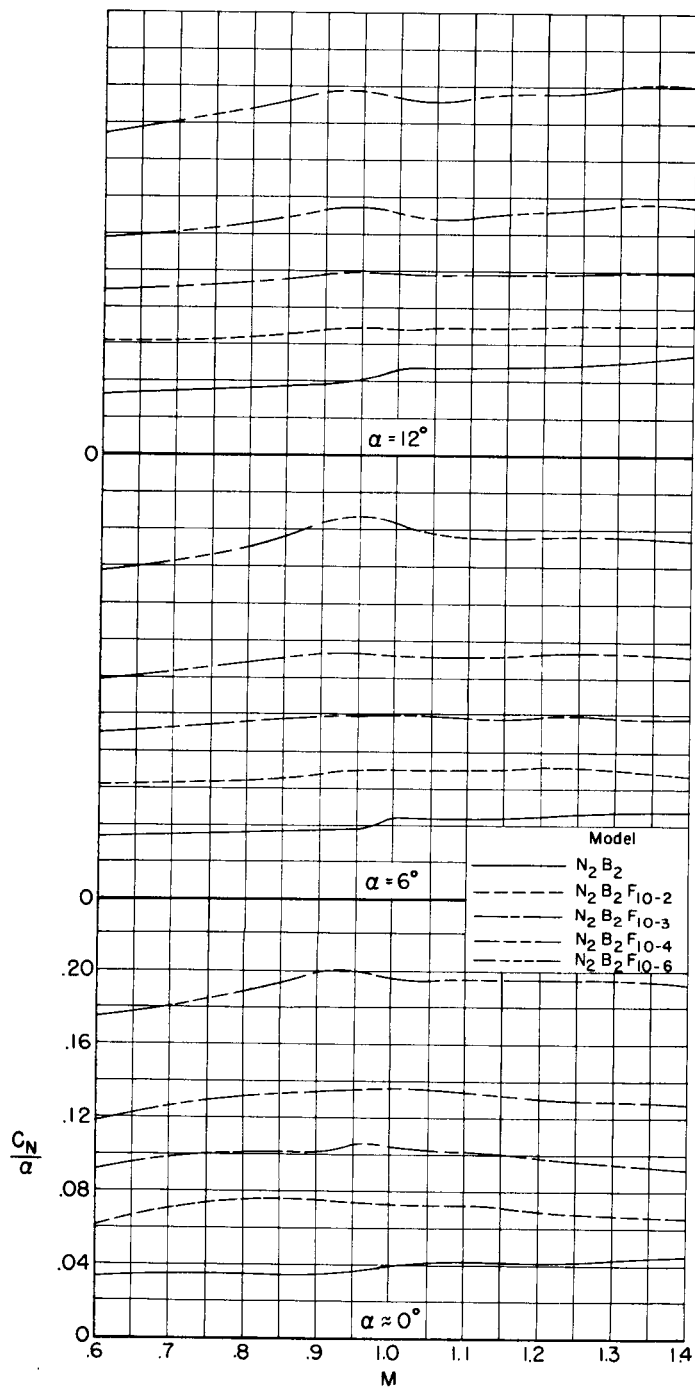
(a) $\theta = 10^{\circ}$

Figure 15.- Effects of flare base area on the normal-force parameter, for constant flare angle.
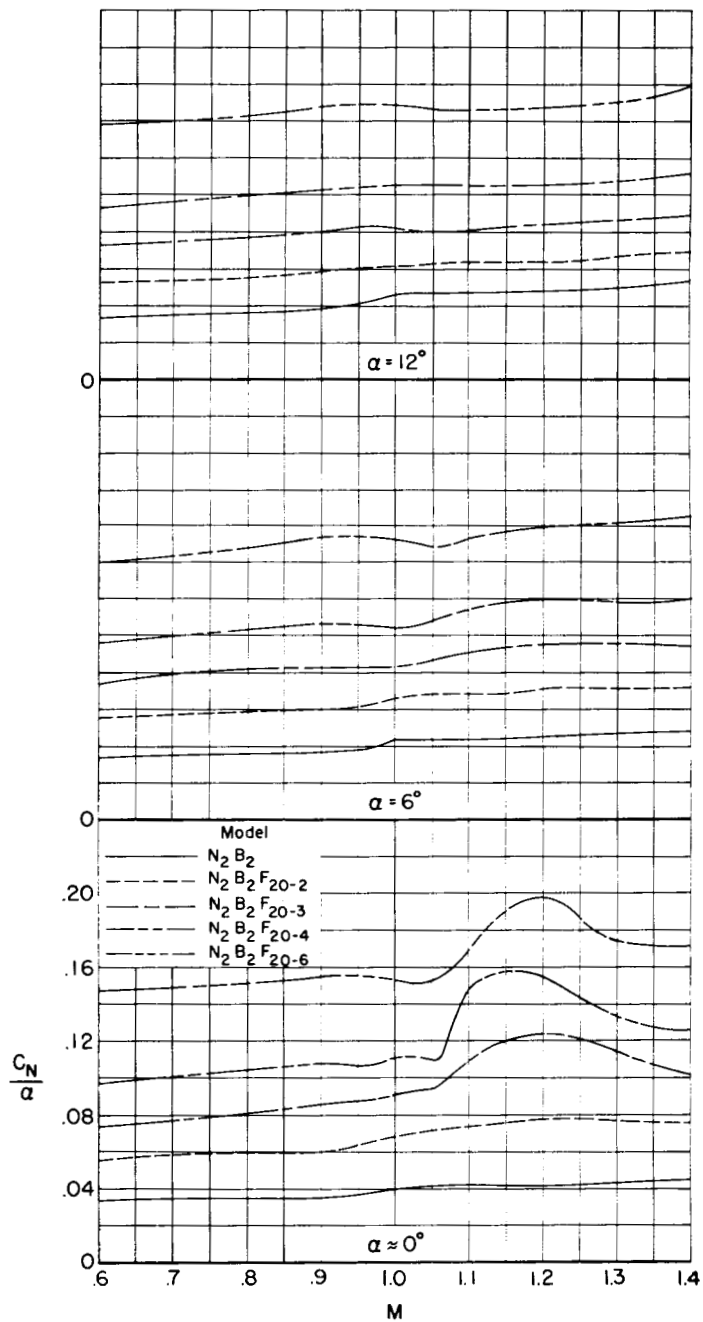
(b) $\theta = 20°$

Figure 15.- Continued.
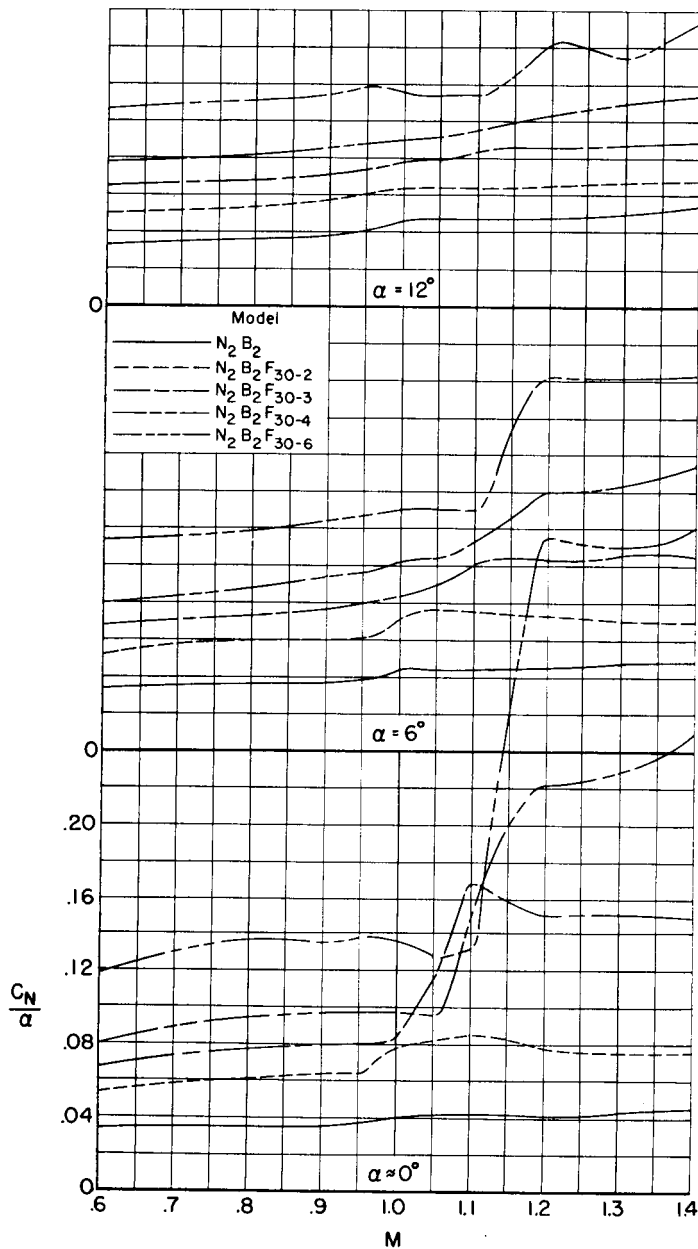
(c) $\theta = 30^{\circ}$

Figure 15.- Concluded.
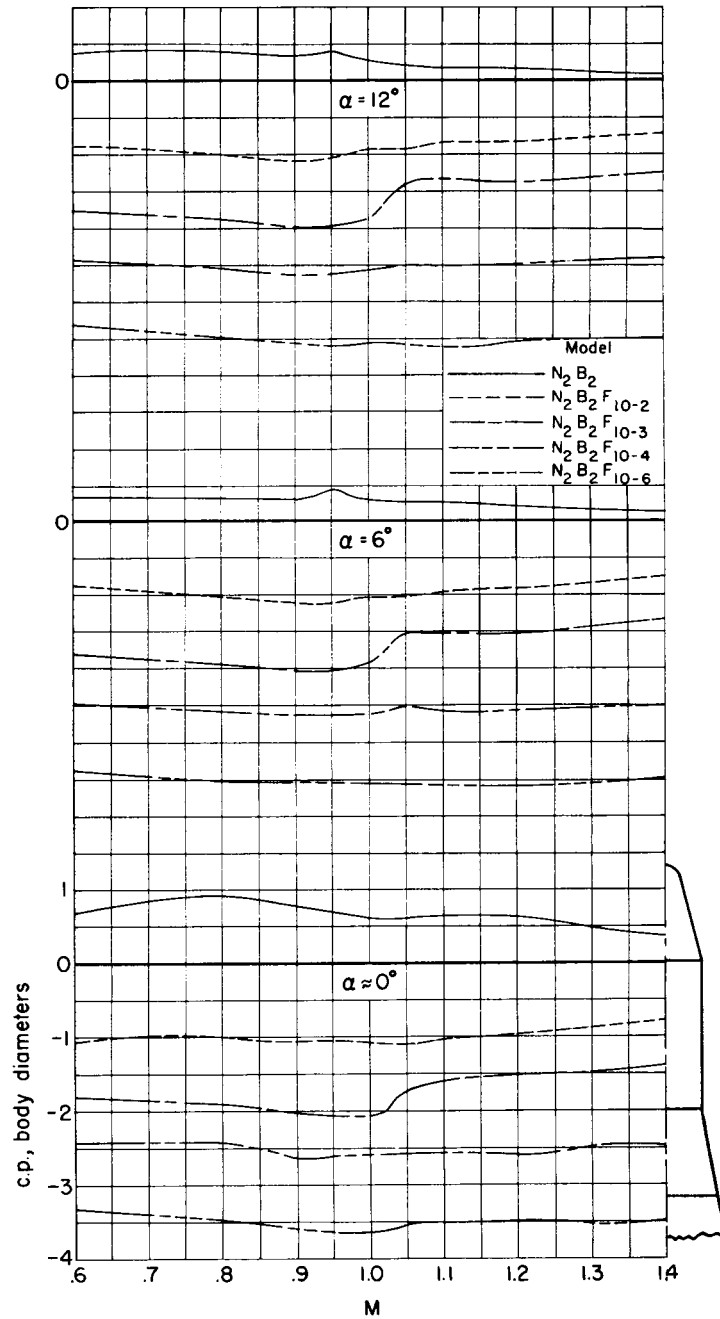
(a) $\theta = 10^{\circ}$

Figure 16.- Effects of flare base area on the center of pressure, for constant flare angle.
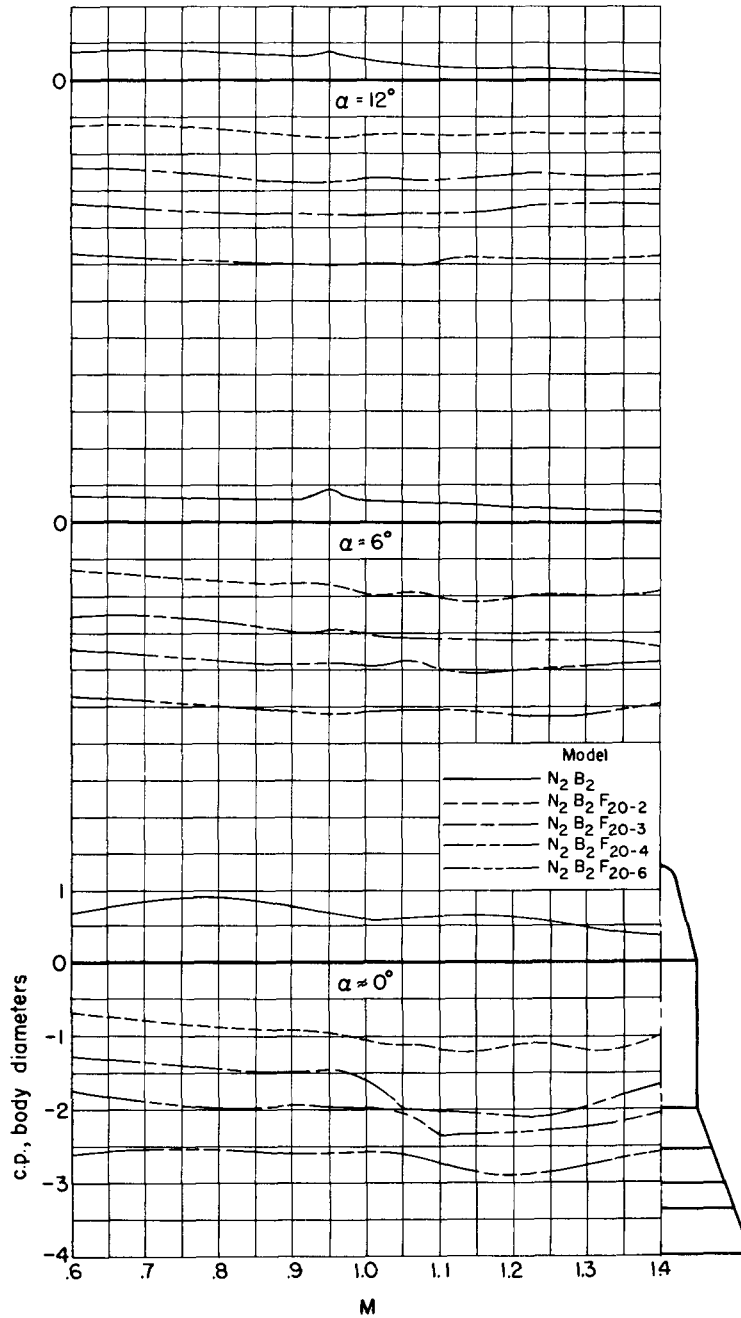
(b) $\theta = 20°$

Figure 16.- Continued.

(c) $\theta = 30^{o}$
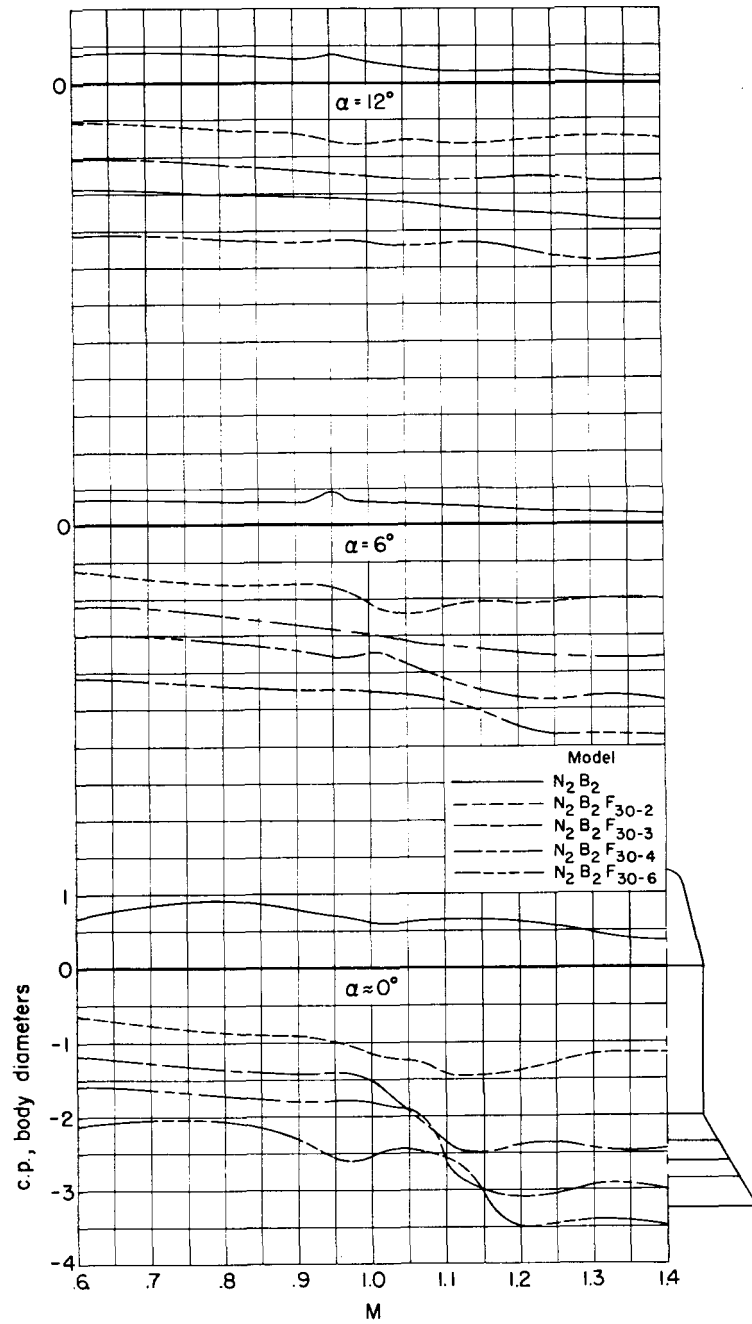
Figure 16.- Concluded.
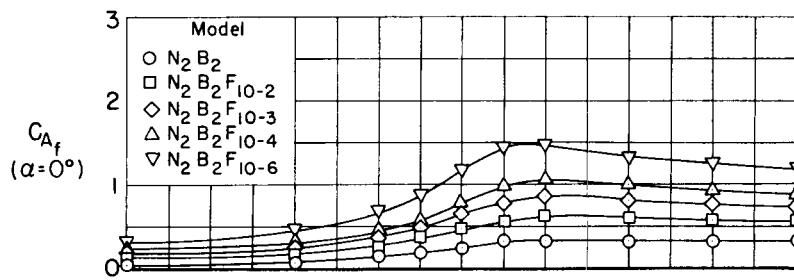
(a) $\theta = 10^\circ$
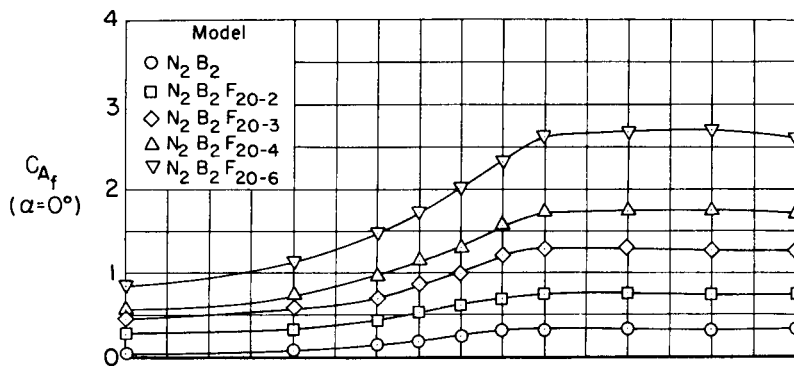
(b) $\theta = 20^\circ$
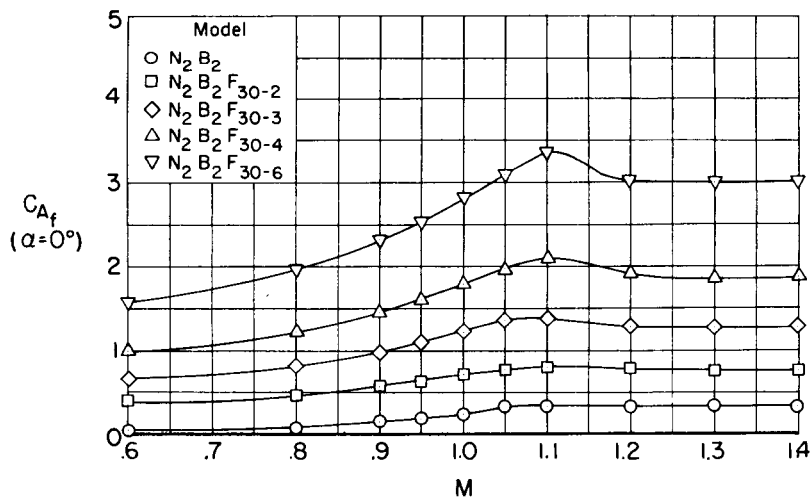
(c) $\theta = 30^\circ$

Figure 17.- Effects of flare base area on the forebody axial-force
coefficient at zero angle of attack, for constant flare angle.
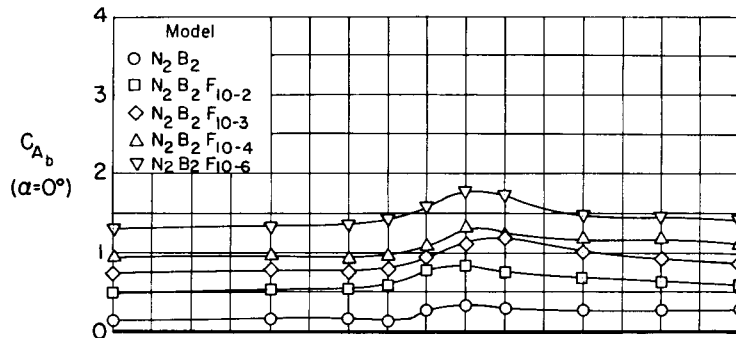
(a) $\theta = 10^\circ$
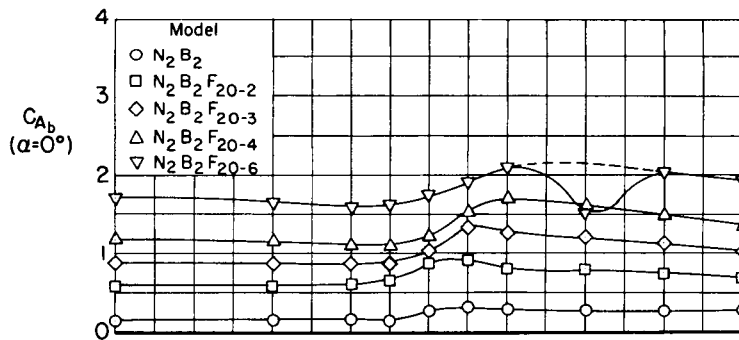
(b) $\theta = 20^\circ$
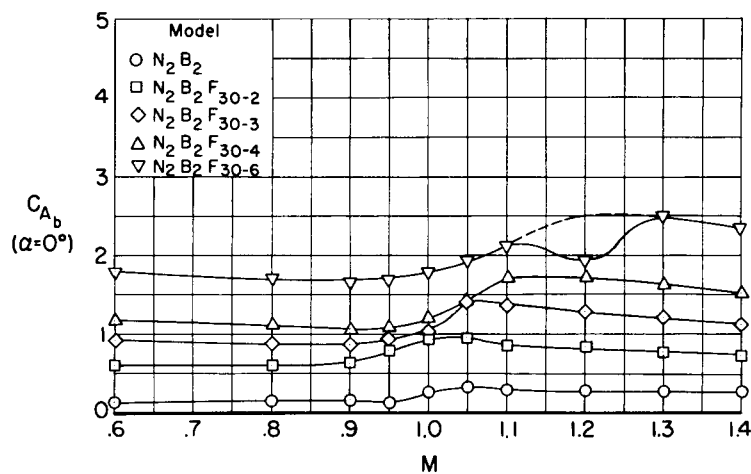
(c) $\theta = 30^\circ$

Figure 18.- Effects of flare base area on the base axial-force coefficient at zero angle of attack, for constant flare angle.
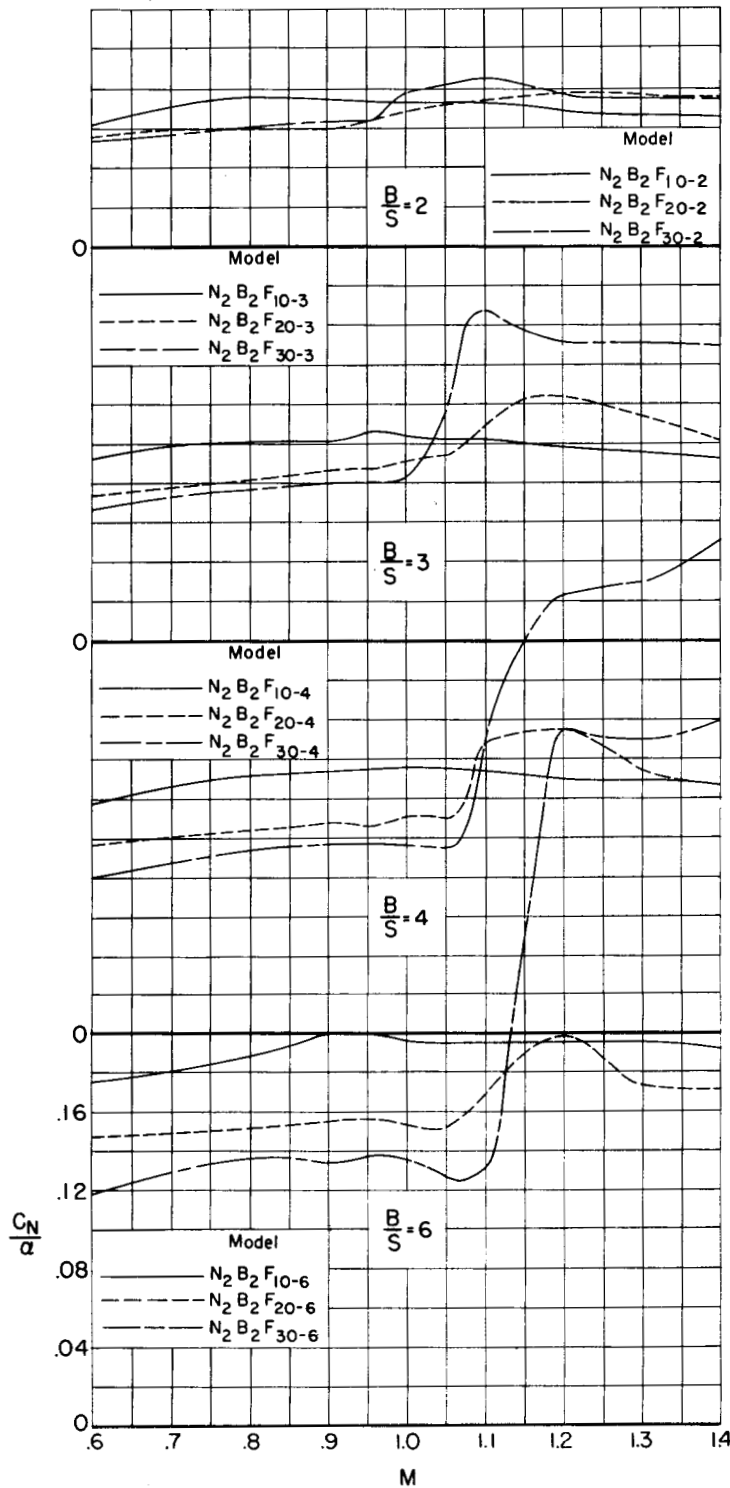
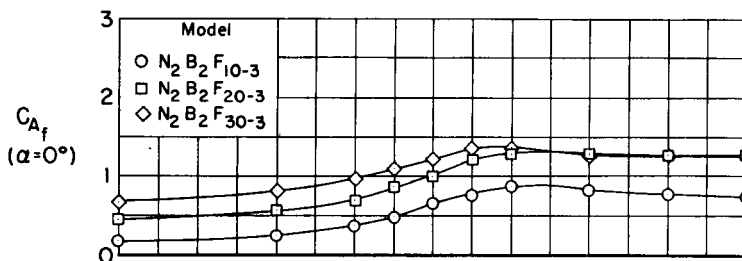Figure 19.- Effects of flare angle on the normal-force parameter near zero angle of attack, for constant flare size.
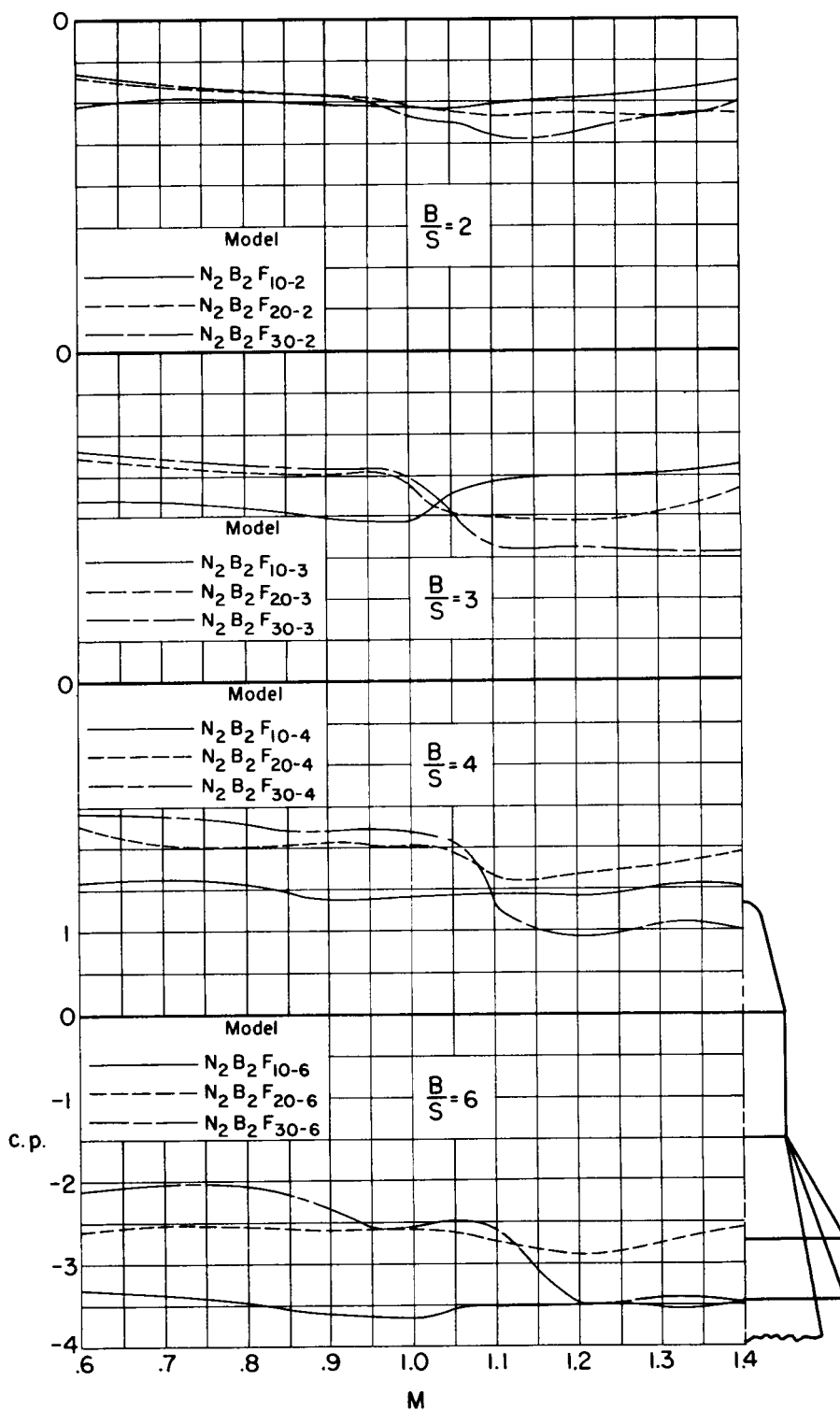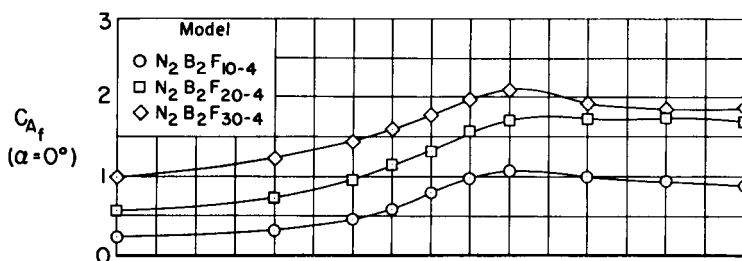
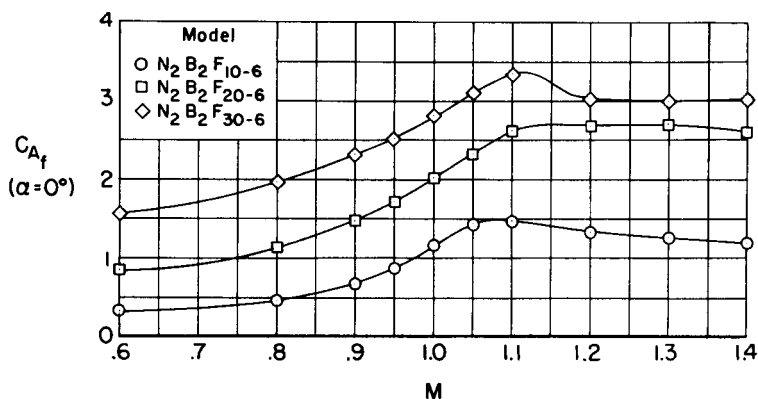Figure 20.- Effects of flare angle on the center of pressure near zero angle of attack, for constant flare size.
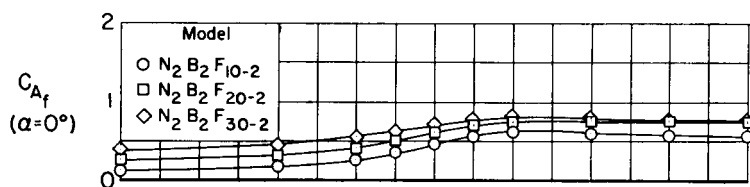
(a) B/S = 2

(b) B/S = 3
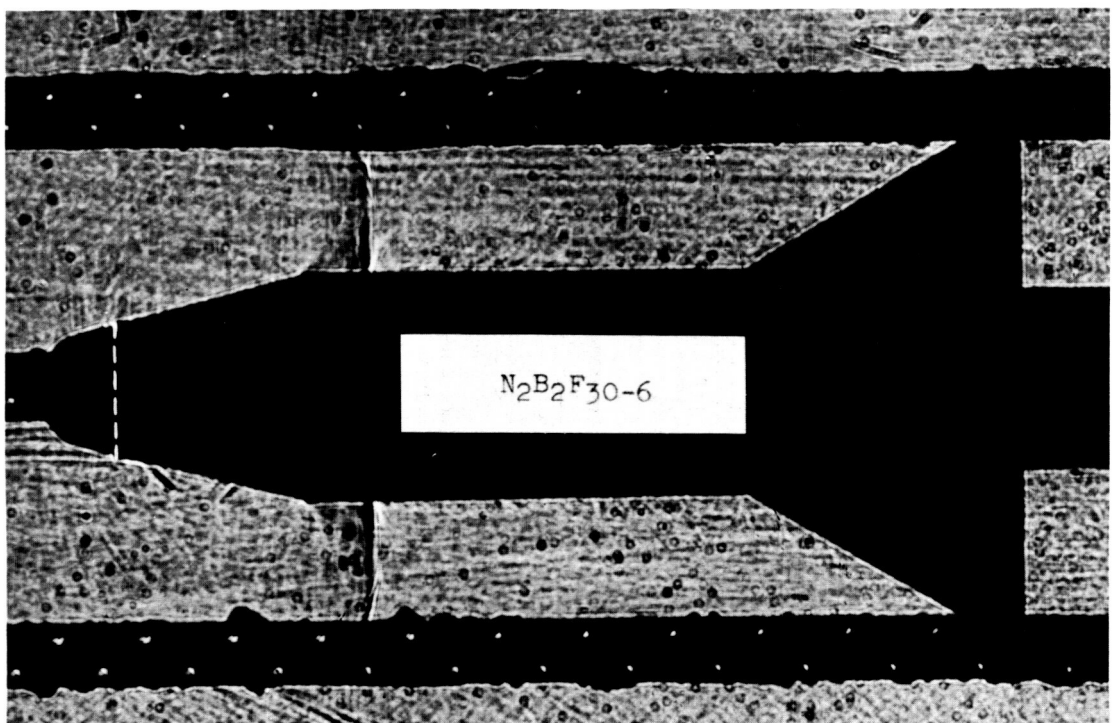
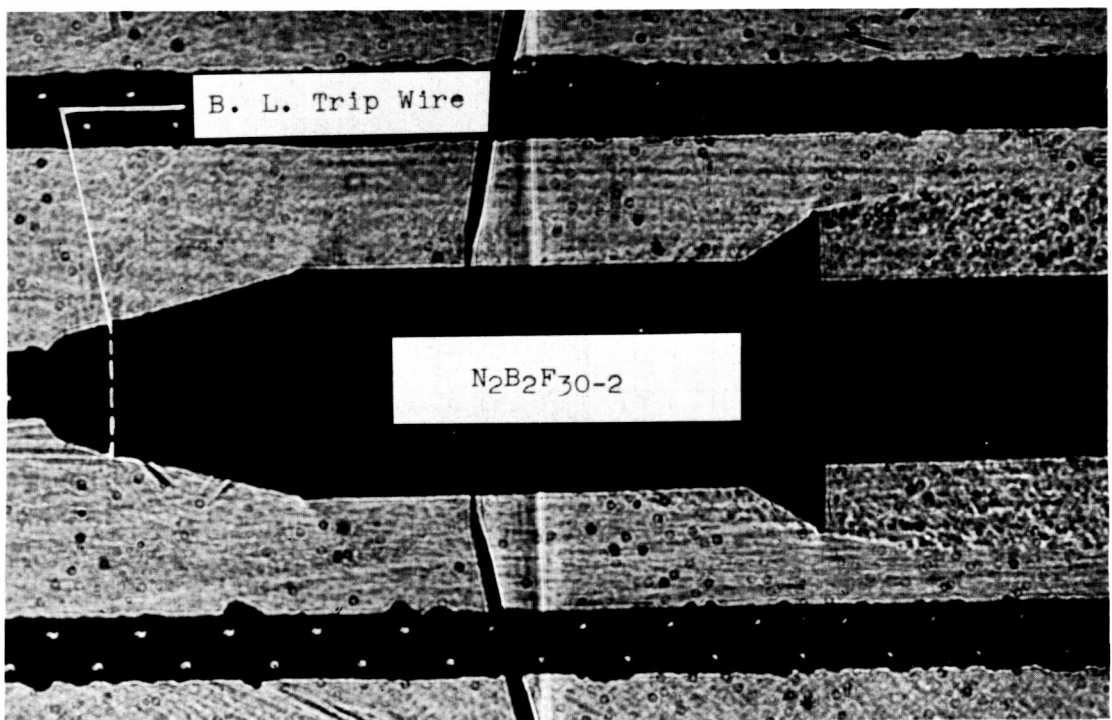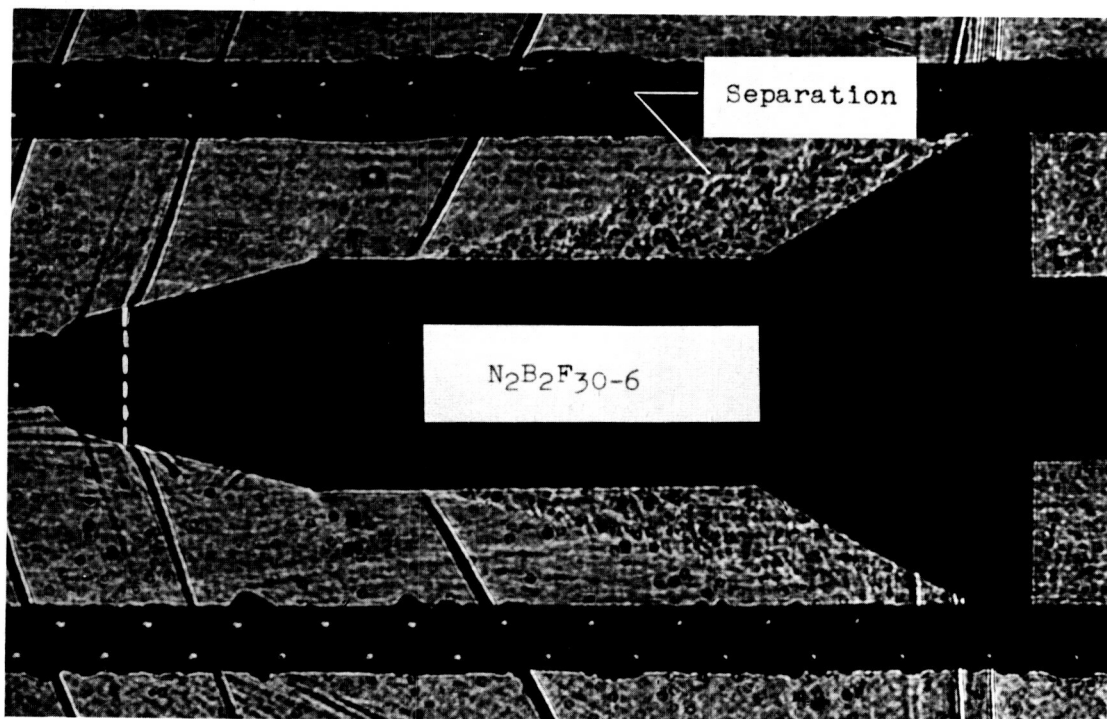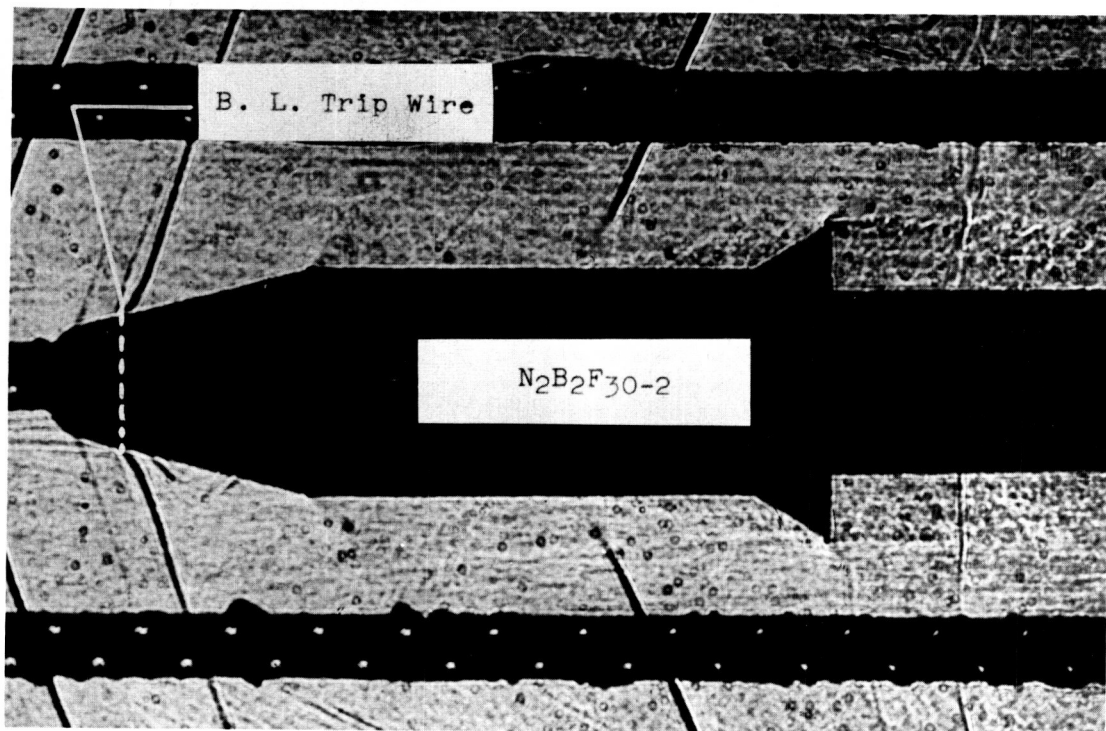(c) B/S = 4

(d) B/S = 6

Figure 21.- Effects of flare angle on the forebody axial-force coefficient at zero angle of attack, for constant flare base area.

B. L. Trip Wire

$N_2B_2F_{30}$-2

$N_2B_2F_{30}$-6

(a) M = 1.00

Figure 22.- Shadowgraph views of two models with 30° flares; $\alpha \approx 0^\circ$.

B. L. Trip Wire

$N_2B_2F_{30}-2$

Separation

$N_2B_2F_{30}-6$

(b) M = 1.20

Figure 22.- Concluded.

CONFIDENTIAL